



JGR Solid Earth

RESEARCH ARTICLE

10.1029/2024JB029191

Key Points:

- Systematic earthquake cycle simulations reveal how subduction zone geometry controls megathrust earthquake size and timing
- Dip and curvature affect characteristic slip style: periodic uniform ruptures versus supercycles of variably-sized slow-to-fast events
- Seismogenic zone dip and dimensions limit maximum earthquake size; curvature-linked stress and strength heterogeneity modulates recurrence

Supporting Information:

Supporting Information may be found in the online version of this article.

Correspondence to:

J. Biemiller, jbiemiller@usgs.gov

Citation:

Biemiller, J., Gabriel, A.-A., May, D. A., & Staisch, L. (2024). Subduction zone geometry modulates the megathrust earthquake cycle: Magnitude, recurrence, and variability. *Journal of Geophysical Research: Solid Earth*, 129, e2024JB029191. https://doi.org/10.1029/2024JB029191

Received 26 MAR 2024 Accepted 3 AUG 2024

Author Contributions:

Conceptualization: J. Biemiller, A.-A. Gabriel, D. A. May, L. Staisch Formal analysis: J. Biemiller, A.-A. Gabriel, D. A. May Funding acquisition: A.-A. Gabriel, L. Staisch

Investigation: J. Biemiller, A.-A. Gabriel, D. A. May, L. Staisch

Methodology: J. Biemiller, A.-A. Gabriel, D. A. May

Project administration: A.-A. Gabriel Resources: A.-A. Gabriel, L. Staisch Software: J. Biemiller, A.-A. Gabriel, D. A. May

Supervision: A.-A. Gabriel, D. A. May, L. Staisch

Visualization: J. Biemiller, A.-A. Gabriel, D. A. May, L. Staisch

© 2024 American Geophysical Union. All Rights Reserved. This article has been contributed to by U.S. Government employees and their work is in the public domain in the USA

Subduction Zone Geometry Modulates the Megathrust Earthquake Cycle: Magnitude, Recurrence, and Variability

J. Biemiller¹, A.-A. Gabriel^{2,3}, D. A. May², and L. Staisch¹

¹U.S. Geological Survey, Portland, OR, USA, ²Institute of Geophysics and Planetary Physics, Scripps Institution of Oceanography, University of California San Diego, San Diego, CA, USA, ³Department of Earth and Environmental Sciences, Ludwig Maximillian University of Munich, Munich, Germany

Abstract Megathrust geometric properties exhibit some of the strongest correlations with maximum earthquake magnitude in global surveys of large subduction zone earthquakes, but the mechanisms through which fault geometry influences subduction earthquake cycle dynamics remain unresolved. Here, we develop 39 models of sequences of earthquakes and aseismic slip (SEAS) on variably-dipping planar and variablycurved nonplanar megathrusts using the volumetric, high-order accurate code tandem to account for fault curvature. We vary the dip, downdip curvature and width of the seismogenic zone to examine how slab geometry mechanically influences megathrust seismic cycles, including the size, variability, and interevent timing of earthquakes. Dip and curvature control characteristic slip styles primarily through their influence on seismogenic zone width: wider seismogenic zones allow shallowly-dipping megathrusts to host larger earthquakes than steeply-dipping ones. Under elevated pore pressure and less strongly velocity-weakening friction, all modeled fault geometries host uniform periodic ruptures. In contrast, shallowly-dipping and sharply-curved megathrusts host multi-period supercycles of slow-to-fast, small-to-large slip events under higher effective stresses and more strongly velocity-weakening friction. We discuss how subduction zones' maximum earthquake magnitudes may be primarily controlled by the dip and dimensions of the seismogenic zone, while second-order effects from structurally-derived mechanical heterogeneity modulate the recurrence frequency and timing of these events. Our results suggest that enhanced co- and interseismic strength and stress variability along the megathrust, such as induced near areas of high or heterogeneous fault curvature, limits how frequently large ruptures occur and may explain curved faults' tendency to host more frequent, smaller earthquakes than flat faults.

Plain Language Summary Subduction zones, where one tectonic plate dives beneath another, generate the largest earthquakes worldwide. Our study investigates how the shape and tilt of these large offshore underground faults, termed "megathrusts," may determine the size of large earthquakes, how often they happen, and how similar or different subsequent events are. By creating computer simulations of earthquakes in subduction zones, we found that the angles and dimensions of the megathrust may set a limit on how big an earthquake can get. We also find that the presence of bends or curves along these faults can make earthquakes more unpredictable, sometimes leading to more variable series of smaller quakes before the biggest one hits. Our findings may help explain why some areas near subduction zones are prone to larger or more frequent earthquakes than others. Understanding these patterns can improve our ability to prepare for these natural disasters, potentially reducing their damaging effects on nearby communities and infrastructure.

1. Introduction

1.1. Mechanical Influence of the Dip and Downdip Width of the Seismogenic Zone

Compelling evidence that the dip angle of the seismogenic zone is a primary factor modulating megathrust seismic cycle dynamics comes from the largest historical earthquakes: $M_w > 8.5$ events have only occurred in subduction zones dipping $<35^\circ$, and $M_w > 9.2$ events have only ruptured megathrusts dipping $<20^\circ$ (Figures 1a and 1b) (Muldashev & Sobolev, 2020; Schellart & Rawlinson, 2013; Wirth & Sahakian et al., 2022). One explanation for this relationship is that the seismogenic zones of shallowly dipping slabs are wider in the downdip direction due to their shallower trajectory through the depth range with temperatures at which offset predominantly occurs via potentially unstable brittle frictional slip (Figures 1d and 1e) (e.g., Bletery et al., 2016; Heuret et al., 2011; Muldashev & Sobolev, 2020; Wirth & Sahakian et al., 2022). Wider conditionally unstable zones should translate to larger areas of the fault that can rupture coseismically and thus, greater potential for large

BIEMILLER ET AL. 1 of 24



Journal of Geophysical Research: Solid Earth

10.1029/2024JB029191

Writing – original draft: J. Biemiller Writing – review & editing: J. Biemiller, A.-A. Gabriel, D. A. May, L. Staisch earthquakes. This relationship is supported by a variety of physical and numerical modeling studies that show fault stability and earthquake magnitude scaling with seismogenic zone width (e.g., Barbot, 2019; Biemiller & Lavier, 2017; Li & Liu, 2016; Liu & Rice, 2005, 2007, 2009; Mark et al., 2018; Muldashev & Sobolev, 2020; Rubin, 2008).

Many features of the earthquake cycle are well-represented by continuum models of elastically deforming lith-osphere around a slipping fault governed by rate-and-state friction and loaded at plate-tectonic rates. Whether modeled faults slip in fast earthquakes, slow-slip transients, or at steady plate-rates depends on the width of the conditionally unstable velocity-weakening portion of the fault, W, and the critical nucleation size h^* , which reflects the critical stiffness for conditional instability of an equivalent spring-slider adjusted by a geometric prefactor based on the dimensionality of the model. In this study, we refer to W as the seismogenic zone width (Figure 1e) and approximate the seismogenic zone as the portion of the fault with velocity-weakening frictional properties (Figure 2f). One form of h^* commonly used in slow-slip cycle models (e.g., Li & Liu, 2016) governed by the aging formulation of rate-and-state friction follows Rubin and Ampuero (2005):

$$h^* = \frac{2Gbd_c}{\pi(1-\nu)(b-a)^2\sigma_n},$$
 (1)

and shows that h^* scales with shear modulus G, Poisson's ratio ν , rate-state friction parameters a and b, critical slip distance d_c , and effective normal stress σ_n . As the ratio W/h^* increases, slip stability transitions from steady creep to transient slow-slip to progressively larger and less frequent periodic earthquakes (e.g., Liu & Rice, 2005, 2007). We note that W/h^* scales directly with the more generalized Dieterich-Ruina-Rice number R_u , = $(b-a)\sigma_u W/h^*$ GL, the most influential of the four primary independent parameters proposed by Barbot (2019) to control seismic cycle dynamics in SEAS models, where L is the characteristic weakening distance and R_n can be negative; W/h^* and R_u represent the same relationships between mechanical properties that determine fault stability. We refer to frictional and mechanical conditions that promote smaller events and steady creep by increasing h^* and driving a given fault's characteristic slip behavior toward the lower end of this W/h^* -controlled slip stability spectrum as more stable, while those that promote larger, less frequent slip events are considered less stable. The critical nucleation size h* represents the fault's stiffness relative to its frictional stability, while W/h* relates the size of the fault's potentially unstable region to this estimate of its inherent frictional stability. Considering a subduction zone with velocity-weakening material distributed over a constant depth range, the primary effect of shallowing fault dip is to increase W, and thus W/h^* , which is expected to drive the fault toward frictional instability and larger earthquakes. Figure 1e schematically illustrates this configuration along with other key subduction zone geometric, frictional, and mechanical factors underpinning potential mechanisms for fault geometry's apparent effects on megathrust earthquake cycles.

Beyond these first-order mechanical consequences of fault geometry, shallowly dipping subduction zones may be subject to unique forces and thermomechanical conditions stemming from the broader geodynamic processes that shape them. For example, subduction of warm and positively buoyant lithosphere may increase on-fault normal stresses, push rheological and frictional stability transitions to shallower depths associated with a warmer geothermal gradient, and shift fluid and pore pressure distributions by enabling fluid-releasing metamorphic dehydration reactions at shallower depths. Slab breakoff or tearing may locally reduce slab pull forces leading to increased normal stresses and decreased shear stressing rates on a shallower megathrust segment, promoting less frequent larger ruptures that occur only once interseismic and dynamic stresses transmitted from steeper neighboring segments overcome its high effective strength. Although it is challenging to decipher how these lithosphere-to-mantle-scale processes influence seismic-cycle-timescale fault dynamics, multi-scale models linking long-term tectonics and geodynamics to the shorter-term evolution of on-fault stress and slip over multiple earthquake cycles have begun to explore these relationships (e.g., Dal Zilio et al., 2019; Lavier et al., 2021). While the complex geodynamic and tectonic history of a region undoubtedly influences its slip partitioning and seismicity in myriad ways, seismic-cycle characteristics and earthquake magnitudes in many multi-timescale models with complex rheologies still depend most strongly on the downdip seismogenic width (e.g., Corbi et al., 2017; Herrendörfer et al., 2015), with additional geodynamic, structural, and mechanical factors only modulating seismogenic potential through their influence on this width. For example, Muldashev and Sobolev (2020) found that subduction of thick packages of weak sediments promoted larger ruptures, but only because the frictional weakness of these sediments pushed the brittle-ductile transition deeper, widening the seismogenic zone.

BIEMILLER ET AL. 2 of 24

21699356, 2024, 8, Downloaded from https://agupubs.onlinelibrary.wiley.com/doi/10.1029/2024/18029191 by Ludwig-Maximilians-Universität, Wiley Online Library on [25/08/2024]. See the Terms and Conditions (https://onlinelibrary.wiley.com/nerms-

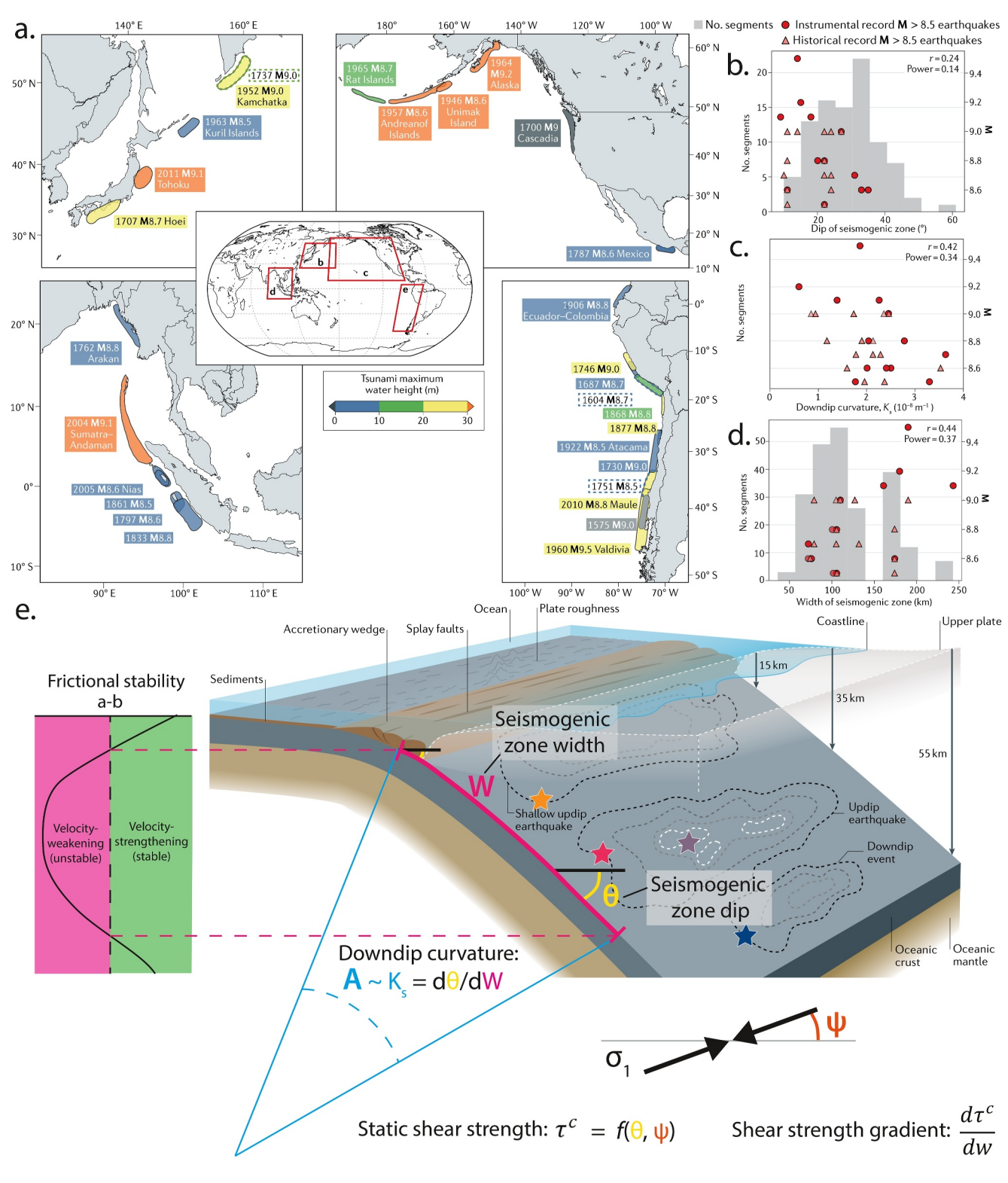


Figure 1.

BIEMILLER ET AL. 3 of 24

1.2. Static and Dynamic Mechanical Effects of Fault Curvature

Global studies showing that historical great earthquake magnitudes also scale with the downdip curvature of subduction zones (Bletery et al., 2016; Plescia & Hayes, 2020; Wirth & Sahakian et al., 2022), with flatter megathrusts hosting larger events (Figures 1a, 1c and 1e), have led to the proposition that fault curvature is the primary geometric factor influencing the maximum rupture size of megathrust earthquake cycles (Bletery et al., 2016). Recent analysis of Slab 2.0 geometries confirms this correlation but posits that observed curvature variations are too small and weak to effectively arrest or limit megathrust rupture propagation (Plescia & Hayes, 2020). We note that in this study we use the term "flat" to describe the local curvature of an interface: a planar fault is perfectly flat with zero curvature (Figure 2b), whereas a "curved" fault is one with nonzero curvature (Figure 2a).

Although few static (e.g., Bletery et al., 2016) and quasidynamic (e.g., Shibazaki et al., 2011; Yu et al., 2018) studies have specifically analyzed mechanisms for downdip slab-scale curvature's effects on subduction zone seismicity, SEAS models of megathrusts composed of curved or kinked segments have shown that similar along-strike variations in fault geometry can act as persistent barriers to rupture (Herrera et al., 2024) or slow-slip event (Li & Liu, 2016, 2017) propagation, which can lead to long-lived along-strike slip segmentation and promote smaller, partial-margin slip events. Bletery et al. (2016) hypothesized that megathrusts' potential to host large earthquakes is largely determined by how spatially variable their static frictional shear strength is: those with smooth homogeneous strength distributions may host larger ruptures because larger portions of the fault can be interseismically loaded close to failure. In contrast, steady loading of subduction faults with larger strength variations over shorter distances will lead to failure of one of the weaker or more strongly locked patches well before much of the fault has been near-critically stressed, nucleating a smaller rupture that arrests once it reaches a strength or stress asperity too strong to propagate through. They express local static fault strength τ^c in terms of dip angle θ , friction coefficient μ , crustal density ρ , depth h, and the angle between the maximum principal stress and horizontal (Figure 1e), ψ , as

$$\tau^{c} = \frac{gh\mu(\rho - \rho_{w})(\sin(2\theta) + \tan(2\psi)\cos(2\theta))}{\sin(2\theta) - \mu(1 - \cos(2\theta)) + \tan(2\psi)(\cos(2\theta) - \mu\sin(2\theta))},$$
(2)

to show that the shear strength gradient, a measure of shear strength heterogeneity, increases with increasing curvature. This relationship supports the hypothesis that the more homogeneous strength of flat megathrusts controls their tendency to rupture in larger earthquakes. In addition to static fault mechanical properties linked to curvature, distinct stress perturbations arise from offsets along curved and planar fault segments in elastic media. Theoretical and modeling studies have shown that fault curvature and roughness primarily affect the normal component of slip-induced tractions (Cattania & Segall, 2021; Chester & Chester, 2000; Tal et al., 2018), resulting in normal traction concentrations at the edges of the curved segment that scale with total slip and local curvature (Romanet et al., 2020).

We hypothesize that the effective loading of a locked megathrust due to deeper interseismic creep may involve a more significant clamping or unclamping (increased or decreased normal traction) component than predicted by planar shear dislocation models, depending on the curvature of the creeping section and the gradient of curvature of the locked-to-creeping transition zone. For example, consider the episodic tremor and slip (ETS) zone downdip of a flat locked seismogenic zone: a slow-slip event (SSE) on a steeply curved section of the ETS zone may clamp or unclamp the updip locked zone more than one on a flatter section would. Similarly, partial ruptures of a curved

Figure 1. Plots modified from Wirth and Sahakian et al. (2022)'s review of great (M > 8.5) subduction zone earthquakes and the mechanical processes and physical properties that influence their occurrence and characteristics. (a) Map of historical and modern great earthquakes from subduction zones around the Pacific. Colorful polygons show inferred rupture areas, with colors indicating maximum tsunami heights. (b–d) Magnitude of historical (pink triangles) and instrumentally recorded (red circles) great subduction earthquakes versus geometric properties of the plate boundary including the dip, downdip curvature, and downdip width of the seismogenic zone, respectively. Gray bars show distribution of geometric properties amongst global subduction zones. Labeled correlation coefficient r indicates statistical strength of the correlation between magnitude and each geometric property. (e) Schematic of the structure and composition of an active subduction zone with representative slip contours outlining seismogenic sources at different depths. Modified labels highlight geometric properties proposed to influence megathrust rupture characteristics and earthquake magnitude, including the dip (θ ; yellow), downdip curvature (which scales with A; blue), and downdip width (W; magenta) of the seismogenic zone. Other potentially rupture-limiting mechanical properties linked to slab geometry include the shear strength and shear strength gradient (τ^c ; $\frac{d\tau^c}{dw}$; black) along the interface and the inclination (ψ ; orange) of the maximum principal stress, σ_I , to horizontal.

BIEMILLER ET AL. 4 of 24

21699356, 2024, 8, Downloaded from https://agupubs.onlinelibrary.wiley.com/doi/10.10292024J8029191 by Ludwig-Maximilians-Universität, Wiley Online Library on [25/08/2024]. See the Terms and Conditions (https://onlinelibrary.wile

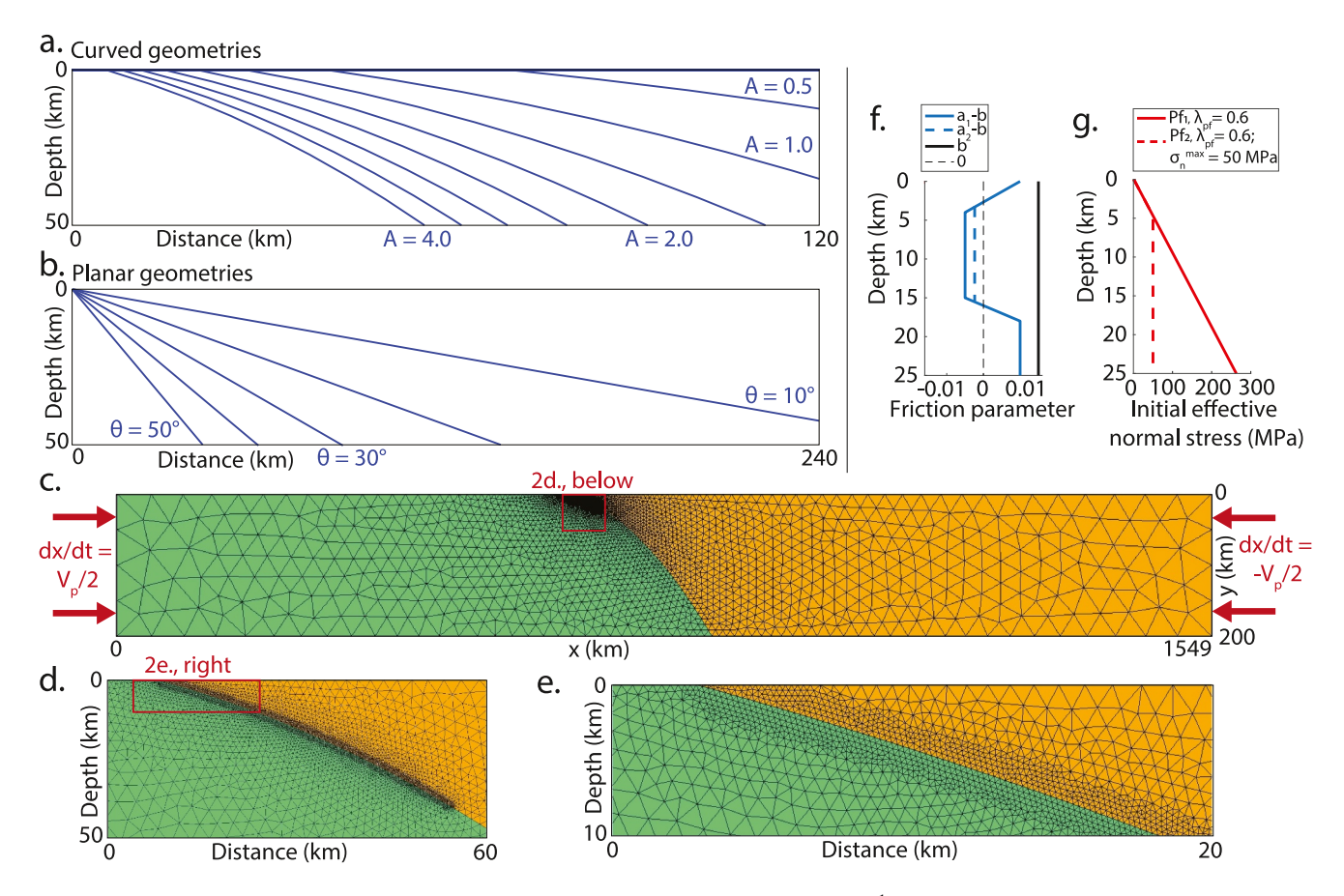


Figure 2. (a–b) Fault geometries of curved (uniform downdip curvature parameter, A, of $0.5-4.0 \times 1,000 \, \mathrm{km}^{-1}$) and planar (uniform dip angle, θ_0 , of $10-50^\circ$) megathrust models, respectively. Curved geometries drawn from Equation 5 with minor vertical offset to avoid fully horizontal segments at the trench. (c–e) Representative mesh and loading of curved models ($A = 1.0 \times 1,000 \, \mathrm{km}^{-1}$). Unstructured triangle mesh of degree 3 curved elements is refined near the frictionally unstable portion of the fault, where edge lengths are <200 m. Steady far-field horizontal convergence is applied symmetrically at the left and right boundaries. Top and bottom boundaries are free. (f) Modeled depth-dependent rate-state frictional parameters for more strongly velocity-weakening (a_1 , model families M/L; Table 1) and less strongly velocity-weakening (a_2 , model family S; Table 1) models. (g) Initial effective normal stresses (red) for models with moderate overpressure at all depths (solid red; $\lambda_{pf} = 0.6$; model family M; Table 1) and with lithostatic pore pressure limiting initial effective normal stress to $\sigma_n^i_{max} = 50 \, \mathrm{MPa}$ (dashed red; model families L/S ; Table 1).

megathrust may impose concentrated normal stress perturbations on neighboring fault patches within their stress shadows, amplifying the effective strength heterogeneity.

1.3. Fault Geometric Complexity in SEAS Models

SEAS models provide insight into how seismic rupture and aseismic creep interact to accommodate steady loading of one or more faults with homogeneous or heterogeneous mechanical properties over multiple earth-quake cycles (e.g., Erickson et al., 2020, 2023; Jiang et al., 2022). In addition to extensive parameter studies that link slip stability and complexity to the relationship between a fault's stiffness and the width of its frictionally unstable zone, as represented by critical instability ratios like W/h^* , R_u or R_b (e.g., Barbot, 2019; Biemiller & Lavier, 2017; Li & Liu, 2016; Liu & Rice, 2005, 2007, 2009; Mark et al., 2018; Rubin, 2008), other studies have investigated how complex non-planar fault geometries affect earthquake cycle slip behaviors. Geometrically complex faults have been approximated in SEAS models by multiple kinked planar segments (e.g., Herrera et al., 2024; Mitsui & Hirahara, 2006; Qiu et al., 2016; Sathiakumar & Barbot, 2021; Sathiakumar et al., 2020) or smoothly kinked subplanar segments (Dal Zilio et al., 2019; Ong et al., 2019), projected surfaces composed of variably-oriented triangular elements (e.g., Li & Liu, 2016, 2017, 2021), smooth fractal distributions of effective normal stress (Cattania & Segall, 2021), or self-affine fractally rough surfaces slipping in a single cycle (Tal et al., 2018; Tal & Hager, 2018). However, limitations of common numerical methods for SEAS simulations typically have not allowed for computationally tractable modeling of many earthquake cycles on smoothly curved plate-boundary-scale faults comprised of curved elements in a curvilinear mesh.

BIEMILLER ET AL. 5 of 24

Newly developed flexible higher-order volumetric finite-element methods (Uphoff et al., 2023) now enable efficient computation of SEAS on two- and three-dimensional faults with curved elements. By constructing curved interfaces from quadratic (or higher polynomial degree) elements and implementing high-order basis functions, these methods allow curved fault surfaces to be represented, rather than approximated by a set of piece wise linear facets, thereby eliminating any potential for numerically induced stress singularities or slip instabilities. Leveraging these new computational techniques, we construct and analyze SEAS models of variably-dipping planar and variably-curved nonplanar megathrusts to systematically analyze how subduction zone geometry influences seismicity over many earthquake cycles.

2. Methods

2.1. SEAS Modeling Numerical Methods: Tandem

In this study, we use *tandem*, an open-source code for 2D/3D earthquake sequence modeling (Uphoff et al., 2023). Tandem solves the elasticity problem with a discontinuous Galerkin finite element method on curved elements in unstructured triangle/tetrahedral meshes. Flexibility and efficiency are provided by defining the displacement evaluation via discrete Green's functions, which are evaluated and checkpoint once in a pre-computation stage using algorithmically optimal and scalable sparse parallel solvers and pre-conditioners. The code is parallelized with MPI and uses linear system solvers from the PETSc-TAO library (Balay et al., 2022) for the static elasticity problem that is solved at each time step. Faults are governed by rate-state friction and adaptive time-stepping permits modeling of coseismic slip, the postseismic period, and interseismic loading across multiple earthquake cycles. We use the quasi-dynamic version of the code and employ degree 4 basis functions. We highlight that we use curvilinear non-planar fault geometry representations which is superior compared with piecewise linear approximations when accurate stresses (or displacement gradients) are required on-fault (Uphoff et al., 2023).

2.2. Model Setup

2.2.1. General Model Description

All our models are 2D and include one fault that crosscuts a rectangular domain (Figures 2a–2c). The fault's updip edge intersects the upper free surface and its downdip edge intersects the bottom boundary, which is also modeled as a free surface. Steady far-field tectonic convergence at plate-rate V_p is applied as symmetric horizontal displacement of the left $(dx/dt = V_p/2)$ and right $(dx/dt = -V_p/2)$ boundaries. To accommodate this convergence, materials in the domain deform elastically in plane strain to an extent determined by their shear rigidity or shear modulus G, compressibility, or Poisson's ratio ν , and density ρ , with initial normal stress $\sigma_n^i = \sigma_n^0 + (1-\lambda_{pf}) \rho gz \le \sigma_n^i{}_{max}$ determined by the pore fluid pressure factor $\lambda_{pf} = P_f/\rho gz$, the background initial normal stress at the free surface σ_n^0 on the order of 1 MPa, and in some cases, a finite maximum initial effective normal stress $\sigma_n^i{}_{max}$ of 50 MPa (Table 1). The resulting elastic strains load the fault, which is modeled as a slipping frictional interface at yield with strength τ^y and instantaneous slip rate V governed by the rate-state friction aging law (e.g., Dieterich, 1979, 1981; Ruina, 1983):

$$\tau^{y} = \sigma_{n} f = \sigma_{n} \left[f_{0} + a \ln \left(\frac{V}{V_{0}} \right) + b \ln \left(\frac{V_{0} \Theta}{d_{c}} \right) \right], \tag{3}$$

for effective normal stress σ_n , instantaneous friction f, reference slip velocity V_0 , state variable Θ , characteristic slip length d_c , reference friction coefficient f_0 , and the direct and indirect friction parameters a and b, respectively. Key processes in this framework are the immediate frictional response to a change in slip velocity known as the direct effect (governed by a), and the more gradual change in "state" and frictional strength over time as surfaces are held in contact known as the indirect or evolution effect (governed by b). The state variable Θ evolves with contact time t according to:

$$\frac{d\Theta}{dt} = 1 - \frac{V\Theta}{d_c}. (4)$$

BIEMILLER ET AL. 6 of 24

 Table 1

 Values of Input Parameters in the Corresponding Models

Parameter	Symbol	Value(s)	Models
Uniform dip angle	θ_{O}	10°-50°; 10° increments	(M/L/S)p10–(M/L/S)p50
Curvature parameter	A	0.5-4.0 (x 1,000 km ⁻¹); 0.5 increments	(M/L/S)c0.5–(M/L/S)c4.0
Plate convergence rate	V_p	3 cm/yr	All
Critical slip distance	d_c	0.05 m	All
Reference friction coefficient	f_{O}	0.6	All
Reference slip velocity	V_{o}	10^{-6} m/s	All
Density	ρ	2.67 g/cm^3	All
Shear modulus	G	32.0 GPa	All
Poisson's ratio	ν	0.25	All
Background normal stress	$\sigma_n^{\ 0}$	1.0 MPa	All
Pore fluid pressure ratio	λ_{pf}	0.6	Mp10-Mp50, Mc0.5-Mc4.0
		0.6–1.0	(L/S)p10-(L/S)p50, (L/S)c0.5-(L/S)c4.0
Maximum effective normal stress	$\sigma_{n\;max}^{\;\;i}$	0	Mp10-Mp50, Mc0.5-Mc4.0
		50 MPa	(L/S)p10-(L/S)p50, (L/S)c0.5-(L/S)c4.0

Note. Model names consist of three terms. The first letter describes the friction and initial normal stress parameters: M, moderate overpressure everywhere with $(a-b)_{min} = -0.005$; L, moderate overpressure transitioning to lithostatic pore pressures at σ^i_{max} with $(a-b)_{min} = -0.005$; S, moderate overpressure transitioning to lithostatic pore pressures at σ^i_{max} with $(a-b)_{min} = -0.003$. The second letter describes the fault geometry: p, planar with uniform dip angle; c, curved with uniform downdip curvature. The final numbers indicate the dip angle $(10-50^\circ)$ or curvature $(0.5-4.0\times1,000~\mathrm{km}^{-1})$.

Frictional stability of a material depends on the sign and value of a-b, which describes the net change in friction due to increased slip velocity. Velocity-weakening materials with a-b < 0 promote unstable slip acceleration like that observed in earthquakes, whereas velocity-strengthening materials with a-b > 0 are intrinsically stable and respond to increased slip rates with increased friction, opposing unstable slip acceleration and rupture propagation. Values of a-b follow a typical stability profile derived from friction experiments on granitic materials and commonly used in simulations of crustal faults, with a shallow velocity-strengthening region transitioning into a velocity-weakening zone at seismogenic depths and back to velocity-strengthening at depths associated with brittle-ductile and viscous deformation (Figure 2f). Stability of the fault interface scales with W/h* (Section 1.1; Equation 1). In this study, W/h* is varied in various ways (Table 1): first, by using different values of W in models with different dip angles and downdip curvatures of the megathrust; second, by varying the pore fluid pressures λ_{pf} that modulate the initial effective normal stresses σ_n^i (Figure 2g); and third, by varying the frictional parameter a in the velocity-weakening zone (Figure 2f).

Fault geometry is assigned to be either planar with constant dip angle θ or concave-down with constant curvature set by the geometric parameter A and the parabolic expression for fault coordinates x and z_i :

$$z_f = Ax^2 (5)$$

which England and May (2021) showed to adequately represent most subducting slab geometries from Slab 2.0 (Hayes et al., 2018). The radius of curvature is related to the second derivative of the function (here 2A); in this study we parameterize, describe, and discuss the downdip fault curvature of interest simply in terms of the curvature parameter A, subsequently referred to as the fault curvature. Planar dips span 10° – 50° and curvatures span A = 0– $4.0 \times 1,000$ km⁻¹ in our models (Table 1), representing the range of global subduction geometries (e.g., Bletery et al., 2016; Wirth & Sahakian et al., 2022). Unique tectonic and thermomechanical conditions likely lead to a range of megathrust frictional stability conditions across global subduction zones. To ensure that modeled effects of variable fault geometry are representative across this spectrum of intrinsic subduction fault frictional stability, encapsulated by h^* , simulations with all fault geometries are performed under three sets of frictional and pore pressure (initial effective normal stress) conditions corresponding to different stability levels. In order of increasing stability (h^*), these three model families (Table 1; Figures 2f and 2g) include: M, moderate overpressure everywhere (Pf_1) with (a_1 - $b)_{min} = -0.005$; L, moderate overpressure transitioning to lithostatic pore

BIEMILLER ET AL. 7 of 24

pressures (Pf_2) at $\sigma_{n\,max}^i$ with $(a_1-b)_{min}=-0.005$; S, moderate overpressure transitioning to lithostatic pore pressures (Pf_2) at $\sigma_{n\,max}^i$ with $(a_2-b)_{min}=-0.003$. Simulations last 10 kyr and the first 5 slip events are excluded from analyses to avoid irregular slip behavior related to the initial loading or "spin-up" phase. Our numerical experiments with tandem represent geometry using a degree three polynomial, hence the interface defined by Equation 5 (e.g., a quadratic function) is exactly reproduced without any numerical approximation error.

2.2.2. Fault Loading Conditions and Variable Normal Stress

Fault loading in SEAS continuum models typically considers only the shear component of elastic tractions resulting from slip or displacement imposed at a constant rate away from the spontaneously slipping portion of the fault. This shear loading can be achieved in different ways, such as by directly applying on-fault elastic shear stressing rates (Biemiller & Lavier, 2017) or, most commonly, by imposing constant slip rates in portions of the fault downdip and/or along-strike of the area of interest, as in the SCEC SEAS community benchmark problems (Erickson et al., 2020, 2023; Jiang et al., 2022). Even when applying such slip-driven loading, finite-domain volumetric methods require specifying the boundary conditions at the edges of the model domain, which can be chosen such that steady far-field displacements match the long-term rigid body motion across the fault (e.g., Erickson et al., 2023). Although neither constant imposed deep slip rates nor constant imposed horizontal convergences rates may perfectly capture the spatiotemporal intricacies of tectonic loading in of natural subduction faults, applying steady slip or convergence rates allows modeled loading rates to be constrained directly from observations and should sufficiently represent first-order tectonic loading for the purposes of earthquake cycle simulations.

Our modeling approach differs from previous studies in two notable ways: (a) we apply kinematic loading by displacing the left and right boundaries of the model domain at a constant prescribed convergence rate and allow the entire fault surface to slip spontaneously as governed by rate-and-state friction laws; (b) we allow both shear and normal stresses on the fault to evolve over multiple modeled slip cycles (Figures 5 and 6) instead of imposing a constant effective normal stress distribution at all times. We assign strongly velocity-strengthening friction to the deeper portions of our faults (~20–200 km depth) such that they gradually creep at near-constant rates, as illustrated by plots of slip rate versus time at different depths from model Mp30 in Figure S1 of Supporting Information S1, similar to the deep steady creep imposed in other 2D dipping-fault SEAS models (Erickson et al., 2023). Computing the time-dependent normal stress evolution enables our models to account for processes such as interseismic clamping and coseismic unclamping of the seismogenic portion of the fault, however it also allows for other effects such as long-term net accumulation or relaxation of normal stresses over multiple earthquake cycles. In most cases, long-term normal stress accumulation decays to minimal rates after adjusting throughout the first few earthquake cycles of each model, which occur during the initial spin-up phase and are discarded from our analyses. This adjustment to relatively steady normal stress levels is evident in the absence of net normal stress accumulation over multiple earthquake cycles in Figure 6.

3. Results

Figure 3 details the evolution of stress and slip over multiple earthquake cycles for two reference models from family M: a planar fault dipping 20° and a curved fault with constant curvature of $3.5 \times 1,000 \, \mathrm{km}^{-1}$. Figures 4–6 show slip-rate, shear stress, and normal stress cycles, respectively, for a selection of 27 planar and curved models with five dip angles and four curvatures from three model families with different pore pressure conditions and frictional properties (Table 1). Figure 7 shows mean coseismic slip at depths above 20 km varies with dip, curvature, and pore pressure for models with a constant moderate pore pressure gradient of $\lambda_{pf} = 0.6$ (family M; Figure 7a) or lithostatic pore pressure above a maximum initial effective normal stress of 50 MPa (family L; Figure 7b). Multi-cycle rupture sequence characteristics are computed for each model and plotted in Figure 9 against various fault geometric properties: W/h^* and the mean dip, curvature, width, and maximum shear strength gradient of the seismogenic zone, which we consider to be the velocity-weakening portion of the modeled faults.

3.1. Characteristic Slip Behavior: Periodic, Quasi-Uniform Earthquake Cycles

While variations in fault geometry, pore pressure, and frictional stability influence many aspects of the resulting earthquake cycles, the relatively homogeneous setups lead to broadly similar slip cycle behaviors shared by most models. The velocity-weakening portions of modeled megathrusts primarily slip during punctuated, unstable slip

BIEMILLER ET AL. 8 of 24

21699356, 2024, 8, Downloaded from https://agupubs.onlinelibrary.wiley.com/doi/10.1029/2024JB029191 by Ludwig-Maximilians-Universitat, Wiley Online Library on [25/08/2024]. See the Terms and Conditions (https://antinelibrary.wiley.com/terms-

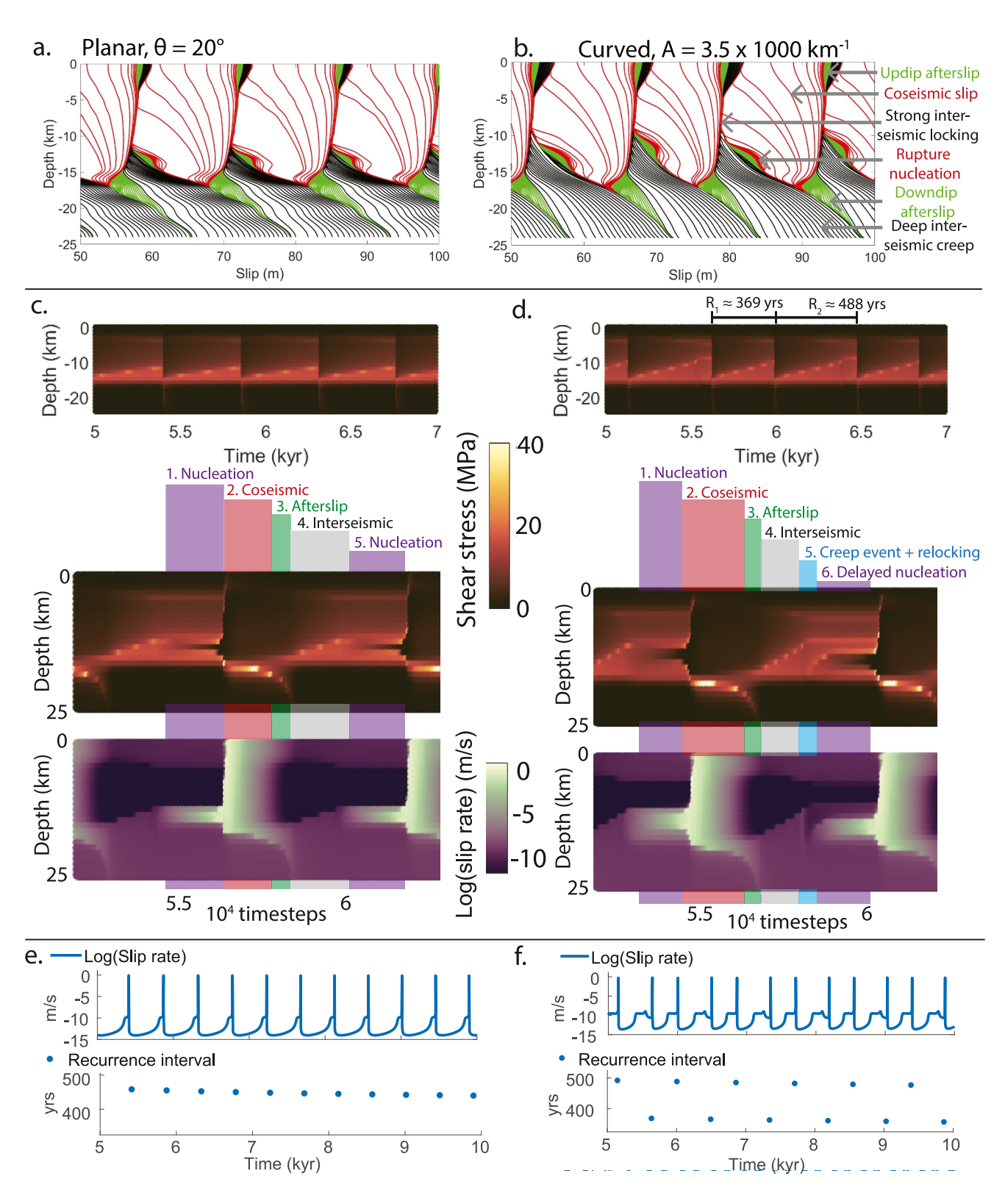


Figure 3.

BIEMILLER ET AL. 9 of 24

events. In most cases, subsequent slip events are similar and repeat periodically following a characteristic recurrence interval. For parameter configurations with sufficiently large W/h^* for seismic instability, ruptures achieve peak slip rates of $\sim 0.1-3$ m/s and host average coseismic slip of $\sim 2-15$ m in the velocity-weakening zone (Figures 7 and 9).

We briefly describe the interseismic, coseismic, and postseismic phases of the characteristic, uniform earthquake cycles emerging in these models. The interseismic phase begins once the accelerated postseismic creep of afterslip has relieved the postseismic stress concentrations left at the updip and downdip edges of the last rupture zone, and creep in the deep velocity-strengthening zone has slowed back down to nearly the plate loading rate (Figures 3c and 3d). As steady far-field convergence continues throughout the interseismic period, shear stress accumulates on parts of the fault that cannot creep fast enough to relieve the applied loading, including the strongly locked velocity-weakening section and the frictional transition zones updip and downdip of it (Figures 2b and 3). As loading persists through the interseismic period, creep in the deep velocity-strengthening section gradually propagates updip following the subtle creep front apparent in Figure 3c, which notably erodes the downdip edge of the locked zone and reduces the width of locking. Similar updip interseismic creep propagation and locking erosion may explain geodetically observed interseismic deformation rates in the Cascadia subduction zone (Bruhat & Segall, 2016, 2017), which is generally considered to be in its late interseismic period (e.g., Walton & Staisch et al., 2021). Continued interseismic loading finally drives most of the partially and fully locked portions to spontaneous failure (Figures 3c and 3d). Rupture propagates updip and downdip from the hypocenter, penetrating most of the fault above ~15 km depth and dissipating most interseismically accumulated stress via rapid coseismic slip. As rupture arrests and the velocity-weakening zone relocks, postseismic stress concentrations updip and downdip of it drive shallow and deep afterslip that gradually decays back to interseismic creep rates.

3.2. Effects of Variable Fault Geometry, Pore Pressure, and Friction

Fault geometry influences multiple aspects of the modeled earthquake cycles. More shallowly dipping and gently curved faults nucleate ruptures near the base of the seismogenic zone, while most of the velocity-weakening zone updip of the hypocenter remains strongly locked throughout the entire interseismic period (Figure 4). Steeper dips and sharper curvature allow the deep interseismic creep front to propagate further updip prior to rupture, leading to shallower hypocenters in the more steeply-dipping and sharply-curved models. These shallowly nucleated events are also smaller: more steeply dipping and sharply curved faults host smaller, more frequent ruptures with less coseismic slip than their shallowly dipping and gently curved counterparts (Figure 8).

Fault geometry modulates the polarity and distribution of cyclic normal stress accumulation and release (Figure 6). Interseismically, curved and more gently dipping planar models tend to accumulate excess normal stress on their shallow locked portions and relieve normal stress on their deeper locked portions. More steeply dipping planar fault models show the opposite polarity of interseismic normal stress accumulation and release: normal stress levels decrease on the shallower portion and increase on the deeper portion. Fault geometry similarly modulates the polarity of coseismic normal stress changes, which mirror the interseismic trends. Coseismic slip tends to relieve normal stress on portions of the fault with interseismically elevated normal stresses and increase normal stress on portions of the fault with interseismically lowered normal stress levels.

In conjunction with pore pressure and friction, fault geometry also affects slip variability, or the degree to which events recur regularly or irregularly in space and time. For the most unstable stress and friction conditions (family M), models with gently-dipping ($\theta_0 = 10^\circ$, 30°) and steeply-curved (A = 3.0– $4.0 \times 1,000 \, \mathrm{km}^{-1}$) megathrusts host quasiperiodic sequences of smaller and larger earthquakes, commonly interspersed with interseismic creep events. For example, the model with constant curvature of $A = 3.5 \times 1,000 \, \mathrm{km}^{-1}$ slips in a distinctly bimodal pattern (e.g., period-two cycles of Barbot, 2019) that regularly alternates between smaller, slower ruptures

Figure 3. (a–b) Cumulative slip contours colored by instantaneous peak slip rate, V_{max} , for planar and curved models with constant dip of 20° or curvature of 3.5 (1,000 km⁻¹), respectively. Red contours representing coseismic phases are plotted every 5 s while $V_{max} > 0.01$ m/s; green contours representing periods of accelerated creep are plotted every 200 timesteps while 0.01 m/s > $V_{max} > 10^{-8}$ m/s; black contours representing interseismic periods of locking and slow creep are plotted every 100 timesteps while $V_{max} < 10^{-8}$ m/s. (c–d) Shear stress accumulation ($\tau - \tau^0$) versus time (top panels) and timestep (middle panels) along with slip rate versus timestep (lower panels) for these planar and curved models, respectively. (e–f) Slip rate, slip, and recurrence interval versus time measured at 12 km depth on the planar and curved faults, respectively.

BIEMILLER ET AL. 10 of 24

21699356, 2024, 8, Downloaded from https://agupubs.onlinelibrary.wiley.com/doi/10.1029/20241B029191 by Ludwig-Maximilians-Universität, Wiley Online Library on [25/08/2024]. See the Terms and Conditions (https://onlinelibrary.wiley.com/erms-and-conditions) on Wiley Online Library for rules of use; OA articles are governed by the applicable Creative Commons Licenses

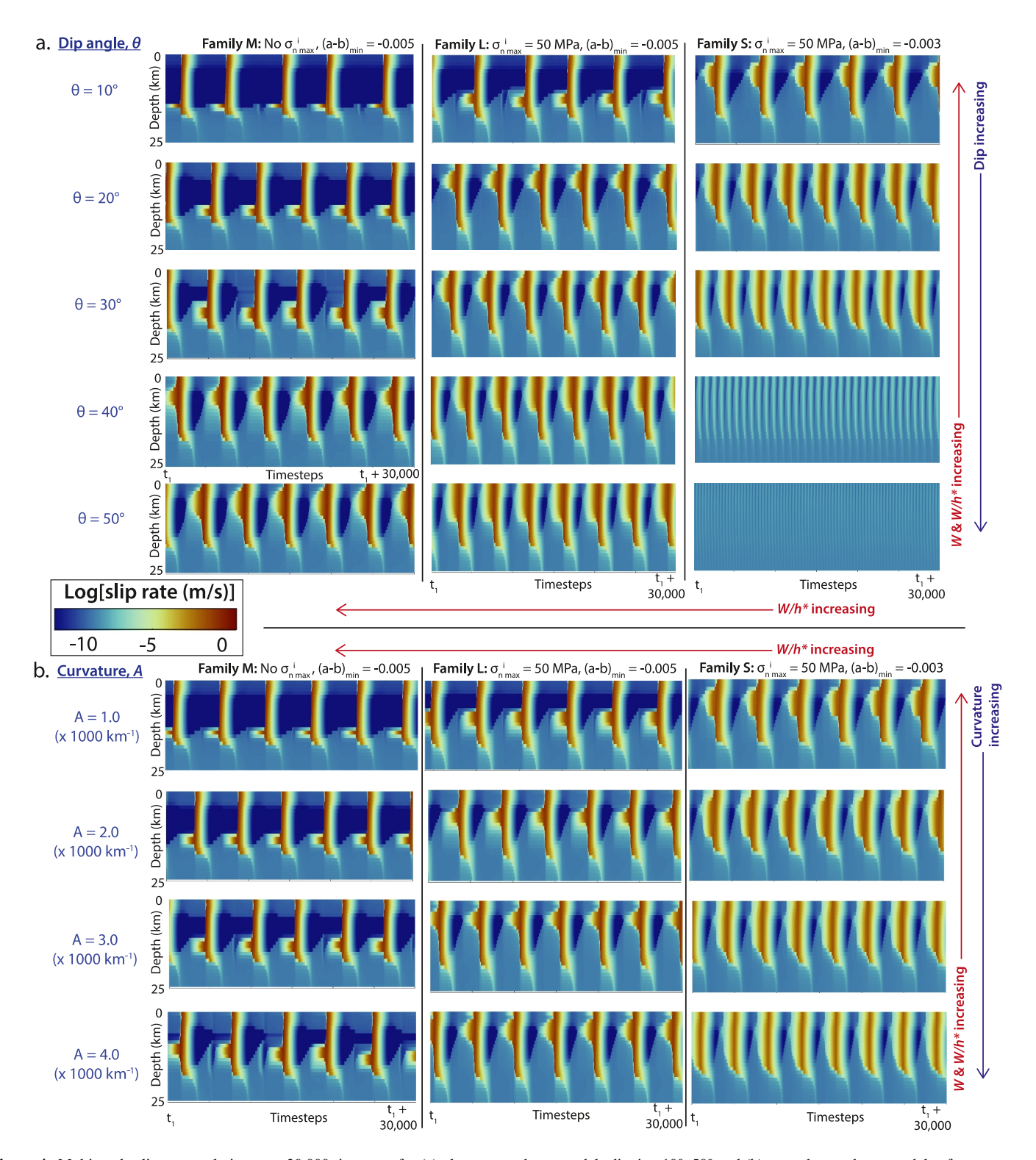


Figure 4. Multi-cycle slip rate evolution over 30,000 timesteps for (a) planar megathrust models dipping 10° – 50° and (b) curved megathrust models of curvatures ranging from 1.0 to $4.0 \times 1,000 \text{ km}^{-1}$ with variable intrinsic stability levels (W/h^* ; red arrows) governed by different initial effective normal stress distributions, a-b values in the velocity-weakening seismogenic zone, and fault dip angles (Table 1; Equation 1).

preceded by interseismic periods of R_1 <375 years and larger, faster ruptures preceded by longer interseismic periods of R_2 >475 years. This bimodality is captured in the model's high recurrence interval standard deviation of >60 years, in stark contrast to the nearly uniform ruptures and recurrence intervals of similar models with steeper

BIEMILLER ET AL. 11 of 24

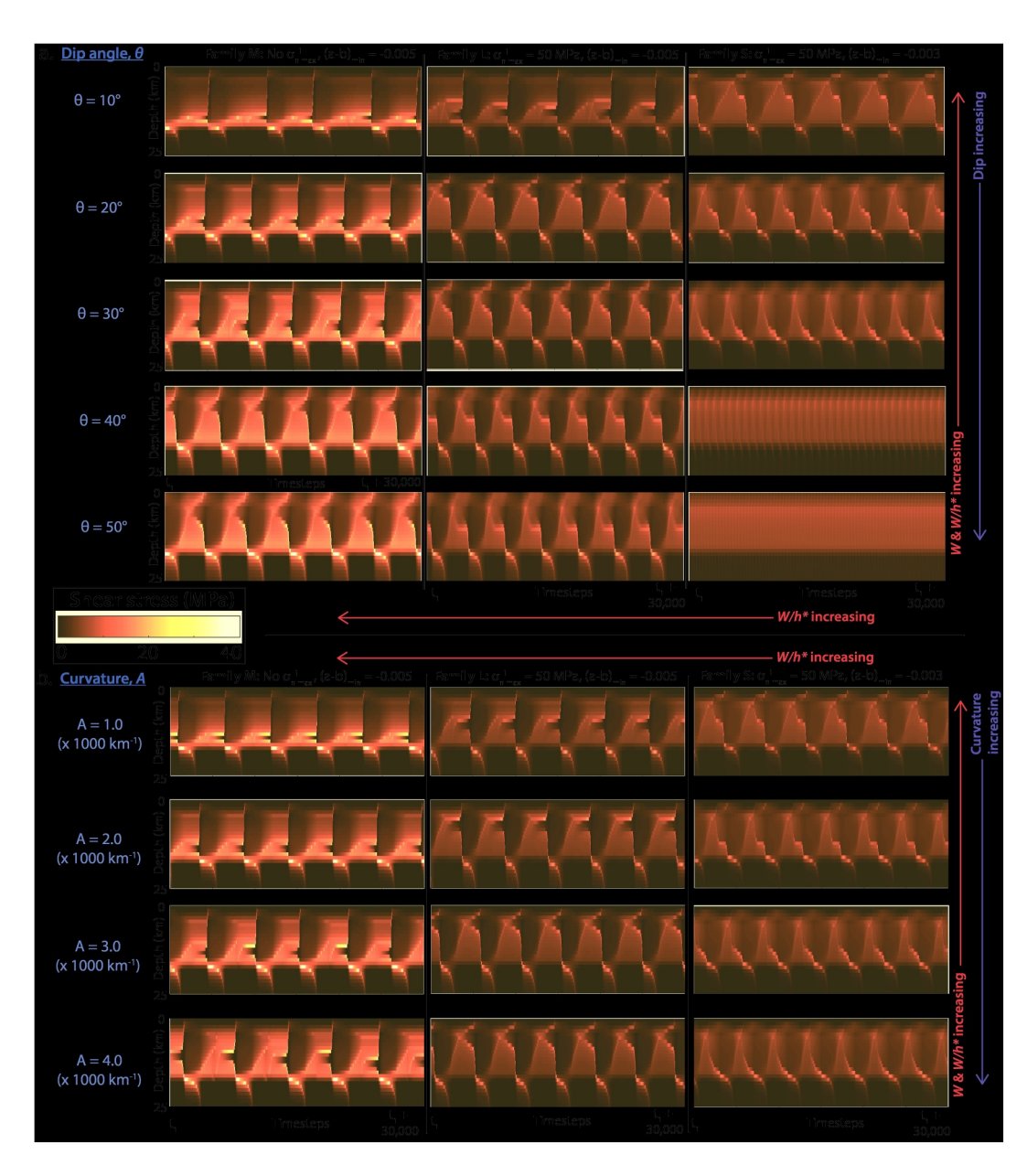


Figure 5. Multi-cycle on-fault shear stress evolution, plotted as instantaneous shear stress minus initial shear stress, over 30,000 timesteps for (a) planar megathrust models dipping $10-50^{\circ}$ and (b) curved megathrust models of curvatures ranging from 1.0 to $4.0 \times 1,000$ km⁻¹ with variable intrinsic stability levels (W/h^* ; red arrows) governed by different initial effective normal stress distributions, a-b values in the velocity-weakening seismogenic zone, and fault dip angles (Table 1; Equation 1).

dips or gentler curvature (Figures 9ea and 9eb). In addition to bimodal sequences, other models with variably-sized ruptures exhibit characteristic repeating patterns of three or five events, while some host more irregular sequences (Figure 8). Enhanced slip variability occurs both in the most shallowly-dipping ($\theta_0 = 10^\circ$; $A = 0.5 \times 1,000 \, \mathrm{km}^{-1}$) and the most sharply-curved ($A = 3.0-4.0 \times 1,000 \, \mathrm{km}^{-1}$) models in family M, suggesting that the emergence of these large-scale creep events is not solely determined by dip or curvature, but instead by the interplay between fault geometry and other stability-linked fault zone conditions such as pore pressure, friction, and stiffness.

This multi-period and more variable rupture behavior is linked to interevent aseismic stress release via spontaneous deep creep events (Figures 3d, 4, and 5) not unlike SSEs (e.g., Rogers & Dragert, 2003). Amidst the longer

BIEMILLER ET AL. 12 of 24

21699356, 2024, 8, Downloaded from https://agupubs.onlinelibrary.wiley.com/doi/10.10292024JB029191 by Ludwig-Maximilians-Universität, Wiley Online Library on [25.08/2024]. See the Terms and Conditions (thtps://onlinelibrary.wie)e.com/terms-and-conditions) on Wiley Online Library for rules of use; OA articles are governed by the applicable Centifying

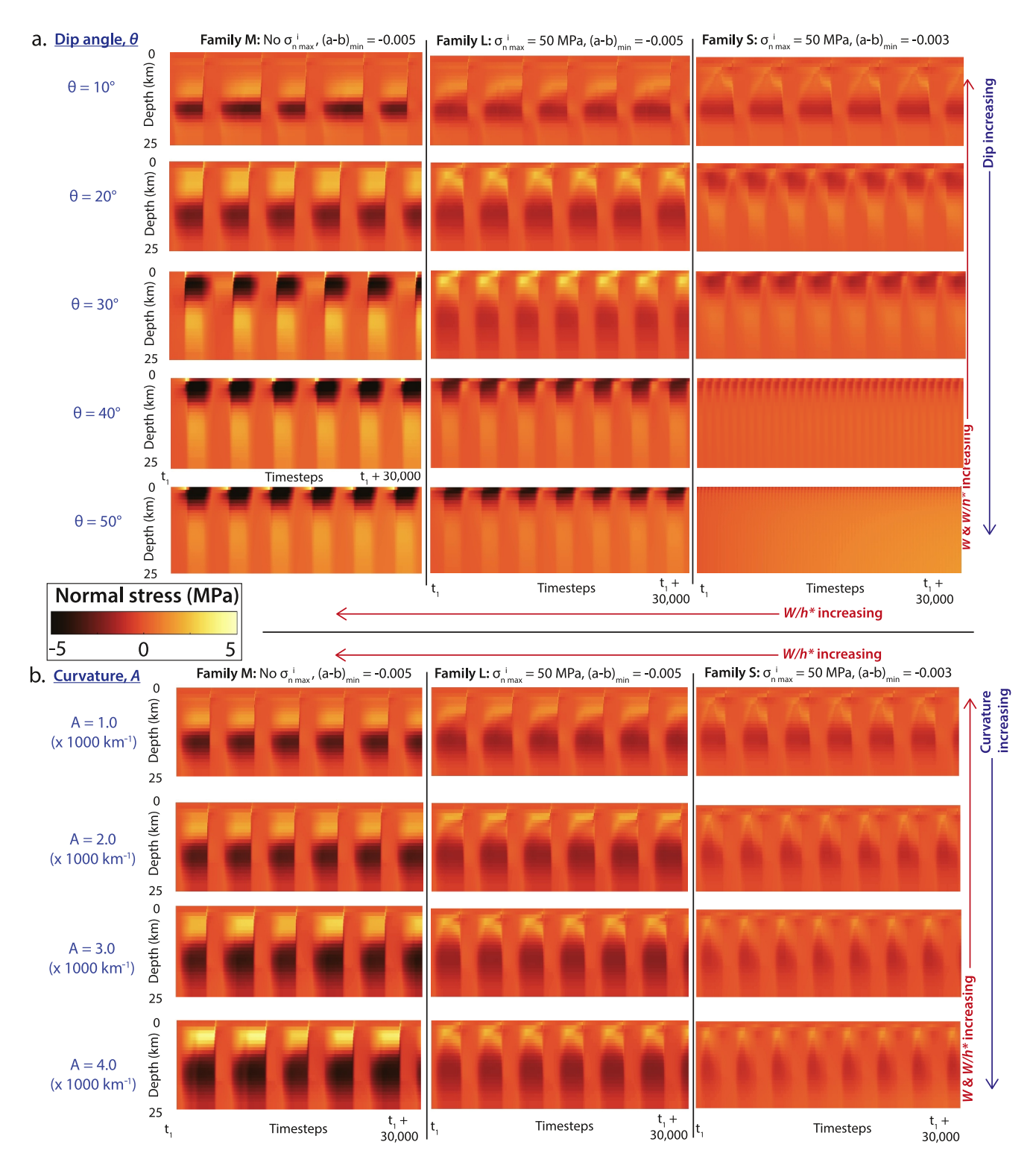


Figure 6. Multi-cycle on-fault normal stress evolution, plotted as instantaneous normal stress minus normal stress at time t_1 , over 30,000 timesteps for (a) planar megathrust models dipping $10-50^{\circ}$ and (b) curved megathrust models of curvatures ranging from 1.0 to $4.0 \times 1,000 \text{ km}^{-1}$ with variable intrinsic stability levels (W/h^* ; red arrows) governed by different initial effective normal stress distributions, a-b values in the velocity-weakening seismogenic zone, and fault dip angles (Table 1; Equation 1).

BIEMILLER ET AL. 13 of 24

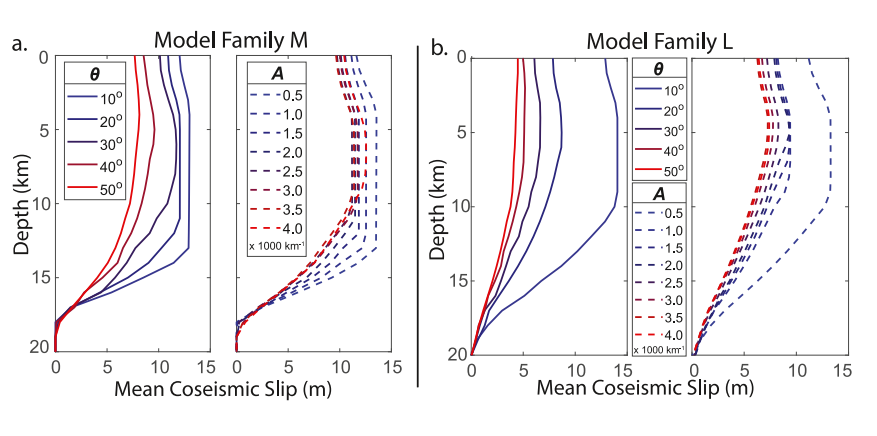


Figure 7. Mean coseismic slip versus depth from planar (left panels) and curved (right panels) models with initial normal stress given by (a) moderate overpressure of $\lambda_{pf} = 0.6$ and no maximum initial effective normal stress (Family M), and (b) moderate overpressure of $\lambda_{pf} = 0.6$ transitioning to lithostatic pore pressure at $\sigma_{n,max}^{\ i} = 50$ MPa (Family L). Predominantly seismic behavior extends deeper on the planar, more shallowly-dipping megathrusts, which also host more coseismic slip per event at most seismogenic depths.

interseismic periods (R_2) of the curved model in Figure 3, for example, the deep transitional portion of the fault downdip of the seismogenic zone hosts a period of faster creep followed by stronger locking (relative to typical interseismic rates) during the late interseismic period. This transient creep event fails to nucleate sustained unstable rupture of the entire fault, but nonetheless appears to relieve interseismically accumulated shear stress in the deeper seismogenic zone and delay subsequent seismic rupture. Figure 8 shows how subtle variations in fault

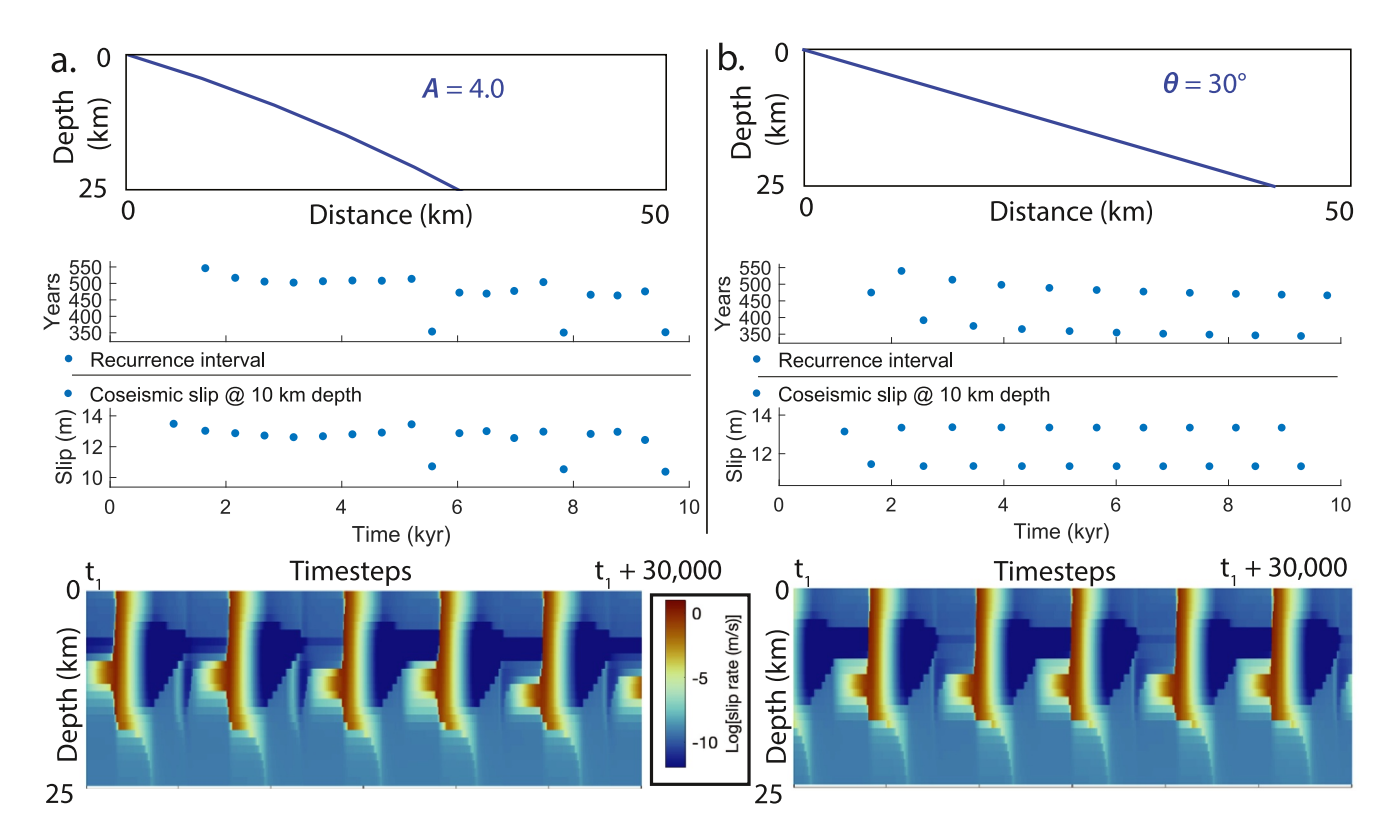


Figure 8. Fault geometry, inter-event recurrence intervals, coseismic slip at 10 km depth, and fault slip rate versus depth for multi-period models from family M with (a) constant curvature of $4.0 \times 1,000 \text{ km}^{-1}$ and (b) constant dip angle of 30° . The flat fault slips in a characteristic alternating pattern of smaller and larger earthquakes, with the larger ones preceded by an interseismic creep event. The curved fault hosts less characteristic slip cycles that include a wider variety of slow-to-fast interearthquake creep events, the fastest of which include or induce transient creep at elevated rates in the shallowest portion of the fault updip of the locked zone.

BIEMILLER ET AL. 14 of 24

21699356, 2024, 8, Downloaded from https://agupubs.onlinelibrary.wiley.com/doi/10.1029/2024JB029191 by Ludwig-Maximilians-Universität, Wiley Online Library on [25/08/2024]. See the Terms and Conditions (https://onlinelibrary.wiley.com/doi/10.1029/2024JB029191 by Ludwig-Maximilians-Universität, Wiley Online Library on [25/08/2024]. See the Terms and Conditions (https://onlinelibrary.wiley.com/doi/10.1029/2024JB029191 by Ludwig-Maximilians-Universität, Wiley Online Library on [25/08/2024]. See the Terms and Conditions (https://onlinelibrary.wiley.com/doi/10.1029/2024JB029191 by Ludwig-Maximilians-Universität, Wiley Online Library on [25/08/2024]. See the Terms and Conditions (https://onlinelibrary.wiley.com/doi/10.1029/2024JB029191 by Ludwig-Maximilians-Universität, Wiley Online Library on [25/08/2024]. See the Terms and Conditions (https://onlinelibrary.wiley.com/doi/10.1029/2024JB029191 by Ludwig-Maximilians-Universität, Wiley Online Library on [25/08/2024]. See the Terms and Conditions (https://onlinelibrary.wiley.com/doi/10.1029/2024JB029191 by Ludwig-Maximilians-Universität, Wiley Online Library on [25/08/2024]. See the Terms and Conditions (https://onlinelibrary.wiley.com/doi/10.1029/2024JB029191 by Ludwig-Maximilians-Universität, Wiley Online Library on [25/08/2024]. See the Terms and Conditions (https://onlinelibrary.wiley.com/doi/10.1029/2024JB029191 by Ludwig-Maximilians-Universität, Wiley Online Library on [25/08/2024]. See the Terms and Conditions (https://onlinelibrary.wiley.com/doi/10.1029/2024JB029191 by Ludwig-Maximilians-Universität, Wiley Online Library on [25/08/2024]. See the Terms and Conditions (https://onlinelibrary.wiley.com/doi/10.1029/2024JB029191 by Ludwig-Maximilians-Universität, Wiley Online Library on [25/08/2024]. See the Terms and Conditions (https://onlinelibrary.wiley.com/doi/10.1029/2024JB02919 by Ludwig-Maximilians-Universität, Wiley Online Library on [25/08/2024]. See the Terms and Conditions (https://onlinelibrary.wiley.com/doi/10.1029/2024JB02919 by Library.wiley.com/doi/10.

and-conditions) on Wiley Online Library for rules of use; OA articles are governed by the applicable Creativ

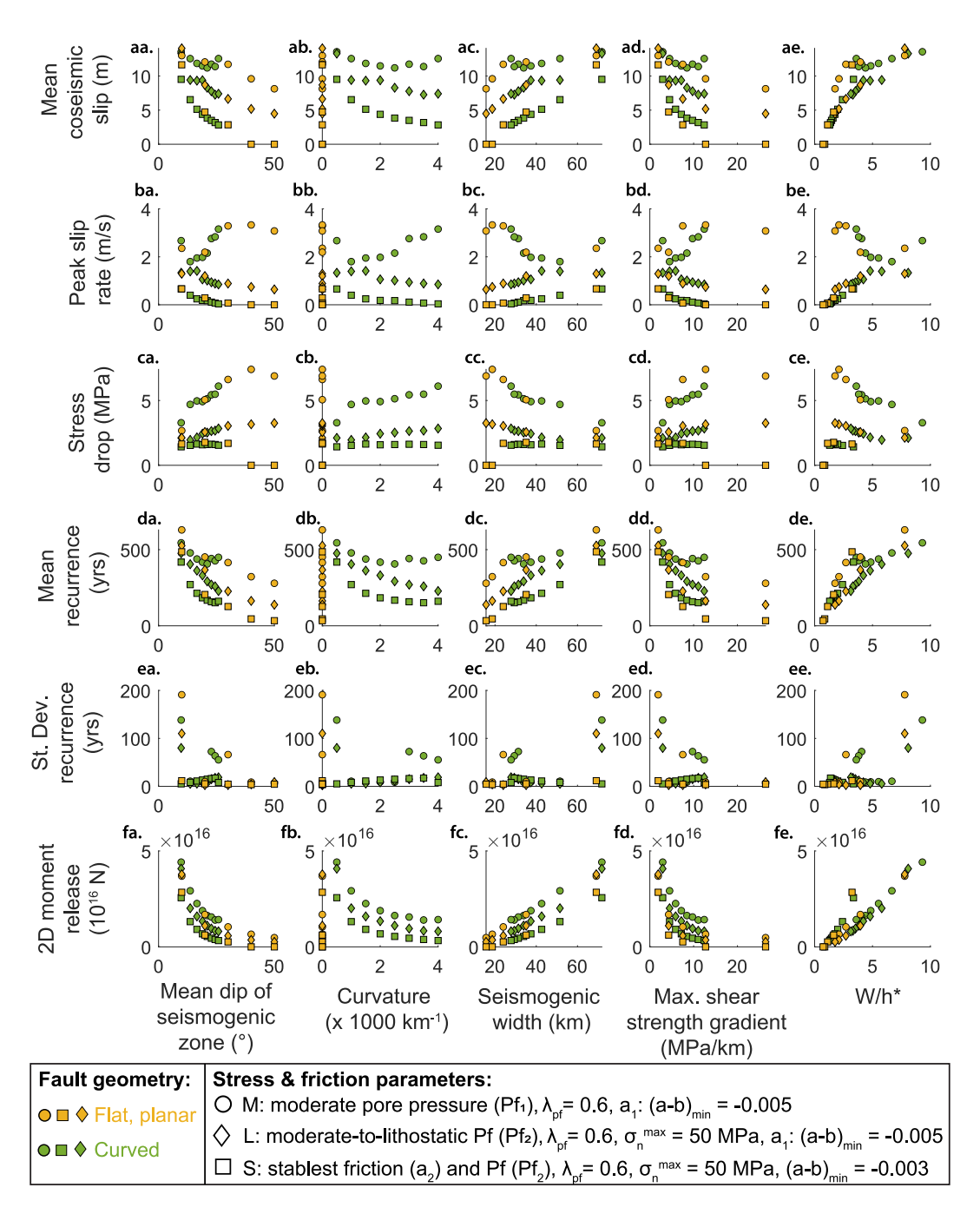


Figure 9. Comparison of geometric properties and modeled rupture characteristics for planar (orange) and curved (green) models with three different sets of frictional stability and initial normal stress parameters (as in Table 1): (1) model family M: uniform moderate overpressure ($\lambda_{pf} = 0.6$) at all depths with (a-b)_{min} = -0.005; (2) model family L: moderate overpressure ($\lambda_{pf} = 0.6$) transitioning to lithostatic pore pressures at $\sigma_{n \max}^i = 50$ MPa with (a-b)_{min} = -0.005; and (3) model family S: moderate overpressure ($\lambda_{pf} = 0.6$) transitioning to lithostatic pore pressures at $\sigma_{n \max}^i = 50$ MPa with (a-b)_{min} = -0.005; and (3) model family S: moderate overpressure ($\lambda_{pf} = 0.6$) transitioning to lithostatic pore pressures at $\sigma_{n \max}^i = 50$ MPa with (a-b)_{min} = -0.005; and (3) model family S: moderate overpressure ($\lambda_{pf} = 0.6$) transitioning to lithostatic pore pressures at $\sigma_{n \max}^i = 50$ MPa with (a-b)_{min}</sub> = <math>-0.005; and (3) model family S: moderate overpressure ($\lambda_{pf} = 0.6$) transitioning to lithostatic pore pressures at $\sigma_{n \max}^i = 50$ MPa with (a-b)_{min}</sub> = <math>-0.005; and (3) model family S: moderate overpressure ($\lambda_{pf} = 0.6$) transitioning to lithostatic pore pressures at $\sigma_{n \max}^i = 50$ MPa with (a-b)_{min}</sub> = <math>-0.005; and (3) model family S: moderate overpressure ($\lambda_{pf} = 0.6$) transitioning to lithostatic pore pressures at $\sigma_{n \max}^i = 50$ MPa with (a-b)_{min}</sub> = <math>-0.005; and (3) model family S: moderate overpressure ($\lambda_{pf} = 0.6$) transitioning to lithostatic pore pressures at $\sigma_{n \max}^i = 50$ MPa with (a-b)_{min}</sub> = <math>-0.005; and (3) model family S: moderate overpressure ($\lambda_{pf} = 0.6$) transitioning to lithostatic pore pressures at $\sigma_{n \max}^i = 0.003$. Resulting rupture characteristics (mean transitioning to lithostatic pore pressures at $\sigma_{n \max}^i = 0.003$. Resulting rupture characteristics (mean transitioning to lithostatic pore pressures at $\sigma_{n \max}^i = 0.003$. Resulting rupture characteristics (m</sub></sub></sub></sub></sub>

BIEMILLER ET AL. 15 of 24

geometry can influence the spatiotemporal patterns and recurrence variability of earthquakes and creep events in these multi-period cycles.

4. Discussion

4.1. Evaluating Individual Geometric Factors That Influence Modeled Megathrust Ruptures

Many modeled rupture characteristics appear to depend relatively monotonically on the geometric properties varied (Figure 9). No geometric property emerges from these models as the singularly dominant factor that controls megathrust rupture behavior. This result suggests that the strong correlations between megathrust geometry and (paleo)seismically recorded great subduction earthquake magnitudes (Bletery et al., 2016; Muldashev & Sobolev, 2020; Plescia & Hayes, 2020; Wirth & Sahakian et al., 2022) reflects the combined mechanical influence of multiple aspects of fault geometry that jointly modulate rupture characteristics like maximum magnitude.

Relatively subtle variations in thermomechanical, lithologic, rheological, structural, tectonic, and loading conditions in SEAS models can influence a fault's characteristic seismic-cycle-timescale slip behavior in complex and interconnected ways. Such heterogeneity-induced slip complexity has been documented in several SEAS modeling studies (e.g., Barbot, 2019; Cattania & Segall, 2021; Liu & Rice, 2007; Rice, 1993; Romanet et al., 2018; Skarbek et al., 2012) and is apparent in the multi-cycle slip-rate and stress records from our variably dipping and curved megathrust models (Figures 4–6). Visualization and qualitative comparison of modeled slip cycles provide a window into the complex relationships between fault geometric or mechanical properties and resulting rupture style (Figures 4–6; e.g., Barbot, 2019; Sathiakumar et al., 2020); nonetheless, more quantitative systematic analysis of representative slip sequence characteristics from these models (Figure 9) can further highlight the strength and scale to which specific geometric properties affect key earthquake cycle behaviors, providing context to global observations of large megathrust earthquakes and subduction zone geometry.

For example, models with higher maximum shear strength gradients, including those with more steeply dipping or sharply curved faults, host more frequent smaller ruptures with less coseismic slip, in agreement with relationships inferred from global compilations of large megathrust earthquakes (e.g., Bletery et al., 2016; Wirth & Sahakian et al., 2022). This result supports Bletery et al. (2016)'s hypothesis that sharper shear strength gradients (i.e., strength heterogeneity) may enhance stress variability, promoting earlier sub-critical failure and more frequent rupture. Similar trends in strength heterogeneity with different geometric properties suggest its effects may be important even when sourced from factors besides fault curvature. The same mechanism proposed to explain slab curvature's influence on maximum earthquake magnitude may also help explain strong correlations between maximum recorded magnitude and other geometric properties like dip, seismogenic width, and W/h* that also scale with maximum shear strength gradient in the seismogenic zone (Figures 9fa, 9fb, 9fd, and 9fe), amplifying the magnitude-limiting effects of fault dip's control over the dimensions of the seismogenic zone. Further observations of megathrust stress and strength heterogeneity, such as those from near-fault borehole observatories (e.g., Chiaraluce et al., 2022) and seismologically inferred coseismic stress reorientations (e.g., Hardebeck, 2015), should be able to test if such heterogeneity exists on the scale predicted by physical and numerical models. Our results suggest that, if so, strength heterogeneity may be a more prevalent and universal mechanism linking fault geometry to earthquake cycle dynamics than previously recognized.

We note that we restrict our models to 2D to isolate the role of each geometric factor and for computational efficiency. Along-strike variability in curvature and dip angle is expected to introduce further heterogeneity (e.g., Bletery et al., 2016; Perez-Silva et al., 2021; Plescia & Hayes, 2020; Schellart & Rawlinson, 2013; Wirth & Sahakian et al., 2022), warranting clear benefit for future 3D modeling efforts. Our models also do not include the effects of other coseismic deformation processes like splay fault rupture and off-fault plastic failure which can play an important role in determining shallow seafloor displacement patterns during megathrust earthquakes, such as the 2004 M_w 9.1–9.3 Sumatra and 2010 M_w 8.0 Maule earthquakes, and should be considered in future modeling studies of large tsunamigenic subduction earthquakes (Biemiller et al., 2022, 2023; DeDontney et al., 2012; Harris, 2004; Ma & Hirakawa, 2013; Ma & Nie, 2019; Melnick et al., 2012; Ramos et al., 2022; Ulrich et al., 2022; van Zelst et al., 2022).).

BIEMILLER ET AL. 16 of 24

4.2. Modeled Slip Variability and Megathrust Geometry

A notable result of our models is the enhanced slip variability (Figures 9ea–9ef) and bimodal earthquake cycle behavior (Figures 3d and 3f) arising for certain fault geometries, particularly under the most unstable pore pressure and frictional conditions (model family M). The most shallowly dipping faults in families M and L slip in multi-period cycles. Yet, family M also hosts complex slip cycles on its 30°-dipping planar and most sharply curved faults (A = 3.0–4.0 × 1,000 km⁻¹) with seismogenic zones similarly dipping 22–26°. Barbot (2019) showed that bimodal (or "period-two") and other multi-period slip styles emerge at intermediate values of $R_b = (b-a)/b$ (for fixed characteristic weakening distance d_c and W/h^*) and at intermediate values of d_c (for fixed R_b). These trends can explain why such variability occurs only in our model families M and L, where $R_b = 0.33$, but not in family S, where $R_b = 0.23$; however, Barbot (2019) does not predict the nonmonotonic trend of multiperiod ruptures with fault dip and curvature, which suggests a more complex relationship between large-scale fault geometry and earthquake cycle complexity.

Previous SEAS modeling studies have linked fault geometric complexity to slip cycle complexity and the emergence of a wider spectrum of slow-to-fast slip transients (e.g., fast creep transients to foreshocks to partial and full ruptures). In some of our models, for example, multi-period earthquake cycles are accompanied by intermittent interseismic deep and/or shallow creep events, which tend to delay the subsequent rupture. Similar slip transient variability has been found to emerge due to along-strike curvature and dip variations (Mitsui & Hirahara, 2006), as well as other types of fault geometric complexity including the proximity of multiple fault segments, as shown in models with two uniform neighboring non-intersecting planar faults (Romanet et al., 2018). Sharper (but not infinitely sharp) kinks and jogs appear to represent stronger, more tightly curved endmember cases of finite-curvature curved fault segments, which may influence earthquake cycle variability through similar mechanisms to those of the subtler curved geometries of our models: Ong et al. (2019) showed that faults comprised of kinked planar segments hosted more frequent earthquakes with less slip than similar ones with smoothly curved transitions between segments. At the megathrust earthquake scale, multimodal rupture behavior controlled by abrupt downdip variations in fault dip has been modeled to explain the two distinct populations of paleoearthquakes recorded along the Main Himalayan Thrust (Dal Zilio et al., 2019). The similar rupture multimodality that emerges in our models suggests that such slip partitioning does not require sharp kinks, but that plate-boundary scale fault geometry can influence earthquake cycle mechanics in a similar manner as smaller-scale bathymetric or structural features do.

Our two groups of multi-period models are distinguished by their shallow or intermediate seismogenic zone dips, suggesting that fault dip is the primary geometric factor responsible for this emergent slip complexity. Nonetheless, fault curvature appears to modulate key aspects of these rupture cycles and their accompanying creep transients. For example, the planar 30° -dipping model hosts regular bimodal ruptures with one self-similar deep creep event preceding each of the larger ruptures, while the similarly-dipping curved model $(A = 4.0 \times 1,000 \text{ km}^{-1})$ exhibits irregular multi-period rupture cycles with most interseismic periods punctuated by variably slow-to-fast deep creep events, the faster of which are accompanied by slower shallow creep events (Figure 7). In the following section, we discuss how fault curvature affects modeled earthquake cycles and discuss possible mechanisms that could explain these effects.

4.3. Earthquake Cycles on Curved and Nonplanar Megathrusts

Beyond modulating these supercycles, megathrust curvature influences certain rupture characteristics across all models (Figure 9, column b). While greater dip and curvature both lead to more frequent smaller events, curved faults generally rupture with less mean coseismic slip after shorter mean recurrence intervals than similarly-dipping but otherwise-identical planar models. Additionally, sharper curvature leads to greater recurrence variability, except in the multi-period models, as shown by the standard deviation of recurrence intervals. These results suggest that even subtle fault curvature introduces mechanical heterogeneity that promotes smaller, more frequent ruptures and potentially enhances slip variability. We examine two possible mechanisms for these effects: (a) elevated static shear strength heterogeneity (Section 4.3.1) and (b) interseismically accumulated stress concentrations linked to lower, more variable fault slip tendency due to enhanced misorientation to regional and/or local tectonic stresses (Section 4.3.2). Finally, we compare these mechanisms to globally recorded slow-to-fast slip behaviors of curved and nonplanar megathrust segments (Section 4.3.3).

BIEMILLER ET AL. 17 of 24

21699356, 2024, 8, Downloaded from https://agupubs.onlinelibrary.wiley.com/doi/10.10292024JB029191 by Ludwig-Maximilians-Universität, Wiley Online Library on [25/08/2024]. See the Terms and Conditions (https://onlinelibrary.wile

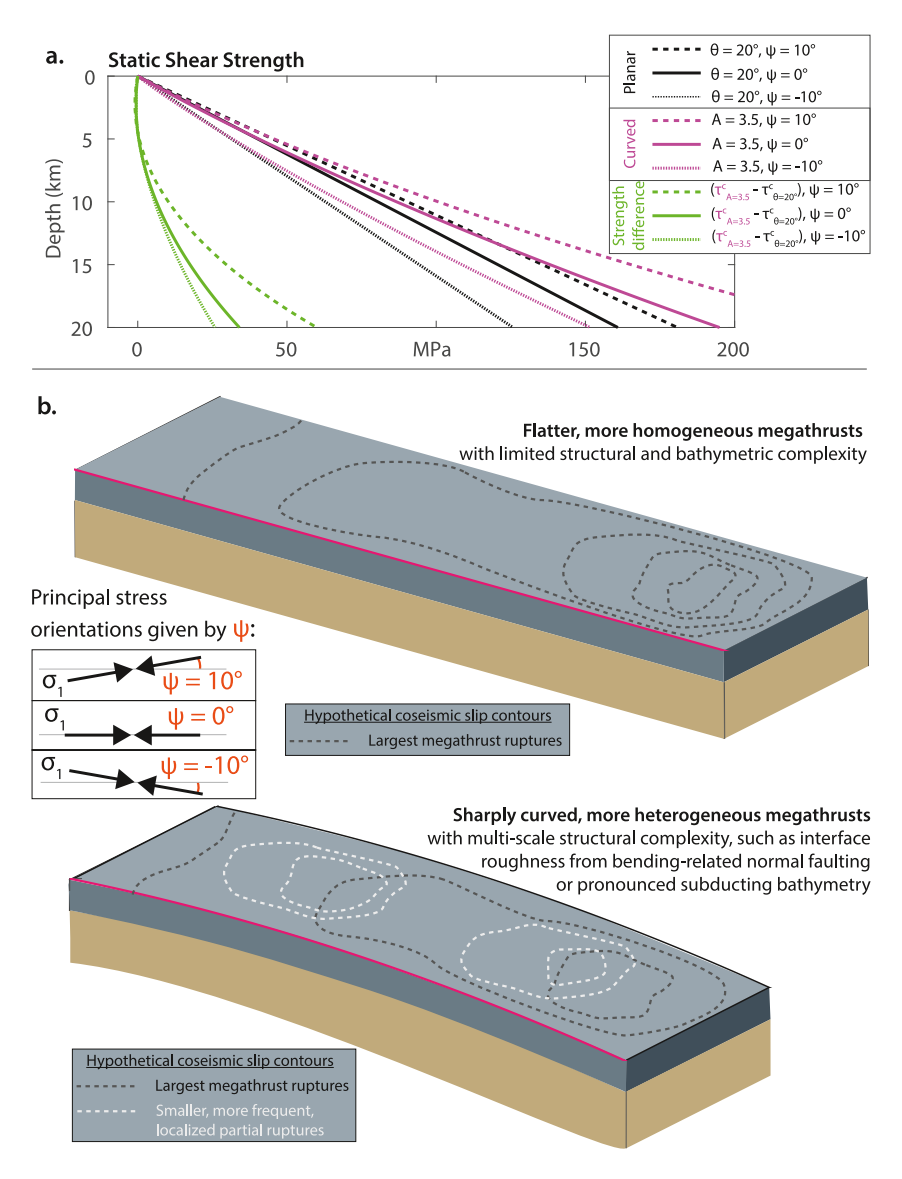


Figure 10. (a) Comparison of static shear strength (Equation 2) with depth for flat planar (black) and curved (purple) models subject to three different maximum principal stress orientations, ψ , as well as the depth-dependent strength difference between these two faults (green). (b) Interpretive schematic slab illustrations based on earthquake cycle processes inferred from 2D modeling results with hypothetical coseismic slip patterns.

4.3.1. Elevated Static Shear Strength Heterogeneity of Curved Faults

In the context of our model results, we first reevaluate static shear strength heterogeneity as a potential primary mechanism responsible for the observationally inferred tendency for flatter megathrusts to host larger great earthquakes. As detailed in Section 1.2, the hypothesis that slab curvature primarily influences large subduction earthquakes by introducing and enhancing static shear strength heterogeneity on the megathrust is mechanically plausible and could explain strong negative correlations between downdip megathrust curvature and maximum recorded earthquake magnitude across global subduction zones (Bletery et al., 2016). Our model results exhibit similar negative correlations between downdip curvature or maximum shear strength gradient and earthquake size (Figures 9fb and 9fd); however, as noted in Section 4.1, they also highlight how shear strength gradient scales with other fault properties, including dip angle (Figures 9fa, 9fd and 10). Higher shear strength gradients of more steeply-dipping faults (Figures 9 and 10) may also help explain similarly strong negative correlations between subduction zone dip and maximum recorded earthquake size globally.

BIEMILLER ET AL. 18 of 24

Next, we consider other components of structurally controlled fault strength that could affect megathrust earthquake cycle dynamics. Beyond local variations in shear strength gradients, shear strength trajectories (Figure 10a) for similar flat and curved faults reveal that uniformly curved faults are statically stronger than their planar counterparts, both locally and in terms of integrated strength over seismogenic depths. Local static strength differences increase with depth and are most pronounced at the base of the seismogenic zone (Figure 10a). The resulting convex-up strength profiles of curved faults could promote more frequent partial ruptures under steady homogeneously oriented loading by enabling smaller updip portions of the fault to be stressed past failure earlier than deeper, stronger parts of the fault that remain subcritically stressed and coseismically locked during these shallower partial ruptures. While subtle differences in maximum shear strength gradients between corresponding planar and curved faults are evident in our models, they are minimal compared to the broader primary trend of shear strength gradients increasing with steepening dip of the seismogenic zone (Figures 9fa, 9fb, 9fc and 10). Moreover, curved faults' relatively higher strength gradient maxima primarily reflect the locally steeper dips of our curved fault geometries at 25 km depth, rather than a broader fault-scale sharpening of shear strength gradients induced by downdip curvature. Given that this mechanism would be expected to function similarly for both geometric properties tested in Bletery et al. (2016) (i.e., dip and downdip curvature), it is not clear that the subtly sharper strength gradients of curved megathrusts relative to the comparably large strength gradients of similarlydipping flat megathrusts are sufficient to control megathrust rupture processes and explain global correlations between subduction zone geometry and maximum earthquake magnitude. Instead, megathrust geometry's primary mechanical effects on subduction earthquake cycles may stem from fault dip through its influence on shear strength heterogeneity and seismogenic widths (maximum rupture dimensions), while second-order effects of curvature-related mechanical heterogeneity more subtly modulate the spatiotemporal evolution and variability of slow-to-fast megathrust slip events in these sequences.

4.3.2. Interseismically Accumulated Stress Concentrations Enhanced by Fault Curvature

While enhanced static shear strength heterogeneity may contribute to the observed and modeled tendency for curved megathrusts to host smaller, more frequent earthquakes, we propose that this effect is amplified by another mechanical process evolving over the earthquake cycle of curved faults: interseismically accumulated stress concentrations due to higher average misorientation of more heterogeneously oriented local fault surfaces relative to more homogeneously oriented stress fields. The hypothesis that curved faults are more poorly oriented to applied stresses relies on an assumption that, at some scale, the principal stress orientations of the local or regional stress field in the surrounding crust are relatively uniform. In a uniform stress field, a flat, planar fault should be better oriented for slip than an identically oriented curved, wavy, or rough fault. Given crustal rocks with Byerlee friction subject to a standard thrust-faulting stress regime with quasiuniform principal stress orientations such that 30°-dipping thrust faults are optimally oriented for slip, a flat megathrust dipping 30° would be overall better-oriented than a smoothly curved megathrust with an average dip of 30° at crustal or seismogenic depths.

In addition to being more poorly oriented to the regional stress field than the central portion, the shallower and deeper portions of the curved megathrust would accumulate positive or negative normal stress concentrations in response to ongoing convergent loading throughout the interseismic period, similar to the positive and negative interseismic normal stress concentrations evident in many of our models (Figure 6). Normal stress concentrations act to clamp or unclamp a fault, effectively increasing or decreasing its local strength. The resulting stress and strength heterogeneity may allow interseismically unclamped areas to nucleate earlier than equivalent areas would on a flat fault, leading to more frequent ruptures with less accrued slip deficit to release coseismically. Romanet et al. (2018) showed that arbitrary imposed slip on a curved fault segment leads to similar normal concentrations adjacent to the segment. If effective, this mechanism of interseismically enhanced stress heterogeneity due to local misorientation should operate similarly at smaller spatial scales, leading to short-wavelength interseismic stress and strength heterogeneity on rough faults or smaller geometric asperities like subducting seamounts. Similar smaller-scale geometric fault roughness modeled by a smoothly varying effective normal stress distribution has been shown to promote foreshock activity and decrease interseismic coupling (Cattania & Segall, 2021).

4.3.3. Possible Links Between Subduction Zone Curvature and Instrumentally Recorded Slow-To-Fast Slip Events

The wider variety and enhanced variability of slow-to-fast slip events arising from our more sharply curved models support previously hypothesized mechanical links between megathrust geometry and slip behavior

BIEMILLER ET AL. 19 of 24

inferred from seismic and geodetic records of slip transients ranging from low-frequency earthquakes and slowslip events to M9+ earthquake ruptures (e.g., Bletery et al., 2016; Bostock et al., 2019; Cruz-Atienza et al., 2021; Dal Zilio et al., 2019; Hardebeck et al., 2015; Hardebeck & Loveless, 2018; Li & Gabriel, 2024; Li & Liu, 2016, 2017, 2021; Melnick et al., 2012; Muldashev & Sobolev, 2020; Ong et al., 2019; Perez-Silva et al., 2021, 2022; Philibosian & Meltzner, 2020; Plescia & Hayes, 2020; Qiu et al., 2016; Sathiakumar & Barbot, 2021; Sathiakumar et al., 2020; Wang & Bilek, 2011; Wirth & Sahakian et al., 2022; Yu et al., 2018). Toward the seismic end of this spectrum, for example, recorded microseismicity rates in the largely flat Cascadia subduction zone are highest in localized areas near sharply curved portions of the interface. Abundant slab and crustal microseismicity below the Puget Sound aligns with a region of high local slab curvature, while similarly intense slab microseismicity occurs in southern Cascadia, where megathrust curvature is highest and most variable due to bending or tearing at the edge of the slab (Bostock et al., 2019). The large-rupture-limiting effects of shorter-wavelength subduction interface geometric heterogeneity or roughness have been identified in, for example, studies of subducting seamounts' influence on seismicity (e.g., Wang & Bilek, 2011). Longer-wavelength structural features have been observed to limit the rupture extent and magnitude of some megathrust earthquakes: coseismic slip in the 2015 M_w 7.8 Gorkha Nepal earthquake was limited to a gently-dipping ~100-km-wide flat segment bounded by steep ramps, indicating that rupture arrested near zones of sharp fault curvature at the ramp-flat transitions (Hubbard et al., 2016; Qiu et al., 2016). Beyond these scales, mechanical links between slab geometry and megathrust earthquake cycles are primarily inferred from paleoseismic records (e.g., Philibosian & Meltzner, 2020; Walton & Staisch et al., 2021).

Mechanical interactions between subduction fault curvature and slower slip transients evident in many of our models (Figure 8) appear to modulate natural slow-slip event characteristics recorded seismically and geodetically in global subduction zones. In the Hikurangi subduction zone, for example, distinct along-strike segmentation between shallow slow-slip patches with different recurrence intervals appears linked to the curved slab segment separating the more shallowly dipping Southern segment with longer recurrence intervals from the more steeply dipping Northern segment with shorter recurrence intervals (Perez-Silva et al., 2022; Wallace, 2020). This tendency for SSEs to occur and be bounded by along-strike transitions in slab dip and curvature was proposed and modeled by Mitsui and Hirahara (2006), who showed that heterogeneous stress accumulation in these curved transition zones promotes quasiperiodic transient creep events. In the Guerrero segment of the Mexican subduction zone, slip in an infamous seismic gap occurs via an array of interacting processes (e.g., Cruz-Atienza et al., 2021; Li & Gabriel, 2024; Perez-Silva et al., 2021) including episodic tectonic tremor (Husker et al., 2012), low-frequency earthquakes (LFEs; Frank et al., 2013, 2014) and SSEs (Frank, 2016; Frank et al., 2015; Kostoglodov et al., 2003), which were recently shown to consist of multiple clustered smaller slip transients accompanied by bursts of microseismicity (Frank et al., 2018). Slip in SSEs terminates in the "transition zone" at a sharp downdip geometric transition from the moderately-dipping shallow portion of the megathrust to a flat subhorizontal section at ~45 km depth. This flat "sweet spot" hosts steady sustained LFE activity, while LFEs in the transition zone occurs in distinct bursts that increase in frequency during and after large SSEs (Frank et al., 2014). Although these small-to-moderate slip transients have been attributed to temporary quasistatic fault weakening related to intermittently elevated pore pressures from migrating pore fluid pulses (Frank et al., 2015), we note that they occur in the vicinity of the most sharply curved section of the frictionally slipping portion of the megathrust and that distinct slip behaviors are observed updip and downdip of this section. Fluid pulses may activate a portion of the megathrust that is geometrically primed for smaller, more frequent, more variable slip transients due to strength heterogeneity in the curved section (e.g., Bletery et al., 2016) or normal stress heterogeneity updip and downdip of it (e.g., Cattania & Segall, 2021; Romanet et al., 2020). Denser instrumentation, longer observations, and global compilations could further test whether interface curvature is strongly correlated with recorded LFEs and SSEs, but observations from multiple subduction zones thus far support the hypothesis that sharper megathrust curvature promotes smaller, more frequent, more variable slip transients.

4.4. Multi-Mechanism Framework for Megathrust Geometry's Influence on Maximal Earthquake Magnitude and Recurrence

Our models illustrate how plate-boundary-scale fault geometry influence slip, stress accumulation and release, and event variability over multiple megathrust earthquake cycles; along with recent models showing that smaller-scale curvature variations and roughness reduce interseismic coupling (Cattania & Segall, 2021) and modulate normal traction concentrations (Romanet et al., 2020; Tal et al., 2018), our results point to multiple links between

BIEMILLER ET AL. 20 of 24

subduction fault geometry, seismic-cycle mechanical heterogeneity, and slip transients across a wide range of spatiotemporal scales.

Inferred mechanisms for fault geometry's influence on megathrust earthquake cycles are summarized in Figure 10, which compares static shear strength between similar flat and curved models alongside schematic diagrams of inferred hypothetical coseismic slip patterns. Strength curves in Figure 10a illustrate how the interplay between downdip curvature, local dip angle and principal stress orientations influence the net relative strength contrast between planar and curved geometries: for all stress orientations, shear strength differences between curved and planar faults increase with depth. Our mechanistic interpretation of these results is summarized in the schematic slab illustrations in Figure 10b: sharper downdip curvature increases both local and megathrust-scale shear strength heterogeneity, as well as the angular deviations between the local fault surface and the maximum principal stress; these deviations prime the fault to develop local interseismic stress concentrations in response to steady uniform loading, which interseismically amplify pre-existing strength heterogeneity. This curvature-enhanced strength and stress variability allows local failure and/or nucleation conditions to be met more frequently across a wider depth range than they would be for a similar flat homogeneous megathrust, leading the curved megathrust to host more frequent and spatiotemporally variable slip events like the partial ruptures illustrated by the light gray contours. Thus, fewer earthquake cycles on a sharply curved megathrust culminate in the largest, full-margin-style ruptures (dark gray dashed contours) than on its planar counterpart, and those that do yield smaller maximal ruptures with less slip and shorter interevent recurrence periods.

An important caveat to this interpretation is that some flavors of slip cycle variability can actually increase the maximum possible earthquake magnitude: for example, the models with multi-period cycles that alternate between smaller and larger ruptures (Figures 3 and 8) yield mean coseismic slip values that fit trends set by the more uniform models, but contain a subpopulation of ruptures larger than those predicted by such trends (e.g., Figure 8). These multi-period cycles are akin to earthquake supercycles documented and inferred from natural fault systems (e.g., Benedetti et al., 2013; Philibosian & Meltzner, 2020), suggesting that fault systems with characteristic supercyclic behavior may be capable of hosting rare ruptures larger than would be predicted by other scaling relationships or other trends. In relation to our models, we emphasize that the curvature-linked mechanical heterogeneity hypothesized and discussed throughout Section 4 are at most second-order effects that modulate earthquake cycles whose primary characteristics appear to be set by fault dip and other dip-dependent mechanical conditions. We closely examined the role of fault dip and curvature in this study, while a broad and thorough investigation of the complex geometric-mechanical interplay that enables such characteristic supercyclic behavior can be found in studies such as Barbot (2019). Future modeling studies incorporating additional geometric complexity such as non-uniformly curved or kinked segments into 3D SEAS simulations could further untangle these geometric and structural controls on megathrust earthquake cycles.

5. Conclusions

We constructed SEAS models of planar and curved megathrusts with varying dip and curvature to systematically test the effects of individual aspects of fault geometry on megathrust slip cycles and rupture characteristics within a consistent modeling framework. Under the most unstable pore pressure and friction conditions tested, certain fault geometries host a wider array of slow-to-fast small-to-large slip transients and exhibited more variance in recurrence intervals and size of modeled earthquakes compared to most other models that primarily host regularly recurring sequences of characteristic slip events. These results support the hypothesis that fault geometry, in conjunction with other physical properties of a fault zone, can control key aspects of slow-to-fast subduction zone slip transients, possibly by modulating static and quasidynamically evolving strength and stress heterogeneity along the interface. Our results indicate that geometrically enhanced shear strength heterogeneity is a key source of mechanical heterogeneity that influences megathrust rupture timing and earthquake size. Furthermore, our results suggest that fault dip may exert a stronger control on shear strength heterogeneity than downdip fault curvature.

Overall, strong relationships between modeled earthquake magnitudes and certain fault geometric properties, such as dip and downdip curvature, align well with strong correlations reported from global surveys of modern and paleoseismic records of great subduction earthquakes. Although average dip and dip-dependent quantities strongly influenced most earthquake cycle characteristics, no single aspect of fault geometry emerged as the sole factor controlling rupture behavior or maximum magnitude. This indicates that relationships between subduction

BIEMILLER ET AL. 21 of 24

Acknowledgments

Primary funding for this work was

provided by a USGS Mendenhall

Postdoctoral Fellowship, a Green

Geology, Minerals, Energy, and

Postdoctoral Scholarship from the Institute

for Geophysics and Planetary Physics at

Scripps Institution of Oceanography, and

the USGS Earthquake Science Center and

Geophysics Science Center. AAG and

DAM acknowledge additional funding

from the National Science Foundation

(Grants numbers EAR-2121568; EAR-

AAG acknowledges additional funding

from the National Aeronautics and Space

Administration (80NSSC20K0495), the

European Union's Horizon 2020 research

and innovation programme (TEAR ERC

Starting Grant number 852992), Horizon Europe (ChEESE-2P Grant number

101093038, DT-GEO Grant number

were provided by the Institute of

Geophysics of LMU Munich (Oeser

conversations from the USGS Powell

Center Cascadia Paleoseismology

imply endorsement by the U.S.

Government.

101058129, and Geo-INOUIRE Grant

number 101058518). Computing resources

et al., 2006). We acknowledge motivating

Synthesis workshop and thank Janet Watt

and John Naliboff for helpful discussions.

Any use of trade, firm, or product names is

for descriptive purposes only and does not

2225286; OAC-2139536; OAC-2311208).

fault geometry and rupture behaviors inferred from natural megathrust earthquakes reflect the combined effects of the unique mechanical contributions from multiple geometric properties including the dip, width, curvature, and stiffness of the frictionally unstable zone. In addition to confirming the first-order role of fault dip, we isolated the second-order effects of fault curvature on modeled earthquake cycle characteristics and proposed two distinct but possibly complementary mechanisms to explain curved faults' tendency to host more frequent, smaller events than flat faults: (a) elevated static shear strength heterogeneity and (b) interseismic accumulation of stress concentrations due to higher average misorientation to applied stresses, leading to and compounded by interseismic enhancement of local strength heterogeneity.

Data Availability Statement

Earthquake cycle simulations were performed using the open-source software *tandem* (Uphoff et al., 2024). All input files required to reproduce the simulations described in this paper are available at the dedicated Zenodo repository (Biemiller et al., 2024).

References

- Balay, S., Abhyankar, S., Adams, M. F., Benson, S., Brown, J., Buschelman, P. B. K., et al. (2022). PETSc/TAO users manual, Tech. rep. Argonne National Lab.(ANL).
- Barbot, S. (2019). Slow-slip, slow earthquakes, period-two cycles, full and partial ruptures, and deterministic chaos in a single asperity fault. *Tectonophysics*, 768, 228171. https://doi.org/10.1016/j.tecto.2019.228171
- Benedetti, L., Manighetti, I., Gaudemer, Y., Finkel, R., Malavieille, J., Pou, K., et al. (2013). Earthquake synchrony and clustering on Fucino faults (Central Italy) as revealed from in situ 36Cl exposure dating. *Journal of Geophysical Research: Solid Earth*, 118(9), 4948–4974. https://doi.org/10.1002/jerb.50299
- Biemiller, J., Gabriel, A.-A., May, D., & Staisch, L. (2024). Subduction zone geometry modulates the megathrust earthquake cycle: Magnitude, recurrence, and variability. Version v2 [Dataset]. Zenodo. https://doi.org/10.5281/zenodo.12588588
- Biemiller, J., Gabriel, A. A., & Ulrich, T. (2022). The dynamics of unlikely slip: 3D modeling of low-angle normal fault rupture at the Mai'iu fault, Papua New Guinea. *Geochemistry, Geophysics, Geosystems*, 23(5), 1–22. https://doi.org/10.1029/2021GC010298
- Biemiller, J., Gabriel, A.-A., & Ulrich, T. (2023). Dueling dynamics of low-angle normal fault rupture with splay faulting and off-fault damage. Nature Communications, 14(1), 2352. https://doi.org/10.1038/s41467-023-37063-1
- Biemiller, J., & Lavier, L. (2017). Earthquake super cycles as part of a spectrum of normal fault slip styles. *Journal of Geophysical Research: Solid Earth*, 122(4), 3221–3240. https://doi.org/10.1002/2016JB013666
- Bletery, Q., Thomas, A. M., Rempel, A. W., Karlstrom, L., Sladen, A., & De Barros, L. (2016). Mega-earthquakes rupture flat megathrusts. Science, 354(6315), 1027–1031. https://doi.org/10.1126/SCIENCE.AAG0482/SUPPL_FILE/AAG0482-BLETERY-SM.PDF
- Bostock, M. G., Christensen, N. I., & Peacock, S. M. (2019). Seismicity in Cascadia. Lithos, 332–333, 55–66. https://doi.org/10.1016/j.lithos.
- Bruhat, L., & Segall, P. (2016). Coupling on the northern Cascadia subduction zone from geodetic measurements and physics-based models. Journal of Geophysical Research: Solid Earth, 121(11), 8297–8314. https://doi.org/10.1002/2016JB013267
- Bruhat, L., & Segall, P. (2017). Deformation rates in northern Cascadia consistent with slow updip propagation of deep interseismic creep.
- Geophysical Journal International, 211(1), 427–449. https://doi.org/10.1093/gji/ggx317
 Cattania, C., & Segall, P. (2021). Precursory slow slip and foreshocks on rough faults. Journal of Geophysical Research: Solid Earth, 126(4), 1–
- 20. https://doi.org/10.1029/2020JB020430
 Chester, F. M., & Chester, J. S. (2000). Stress and deformation along wavy frictional faults. *Journal of Geophysical Research*, 105(B10), 23421–23430. https://doi.org/10.1029/2000JB900241
- Chiaraluce, L., Festa, G., Bernard, P., Caracausi, A., Carluccio, I., Clinton, J. F., et al. (2022). The near fault observatory community in Europe: A new resource for faulting and hazard studies. *Annals of Geophysics*, 65(3), 1–17. https://doi.org/10.4401/ag-8778
- Corbi, F., Herrendörfer, R., Funiciello, F., & van Dinther, Y. (2017). Controls of seismogenic zone width and subduction velocity on interplate seismicity: Insights from analog and numerical models. *Geophysical Research Letters*, 44(12), 6082–6091. https://doi.org/10.1002/2016GL072415
- Cruz-Atienza, V. M., Tago, J., Villafuerte, C., Wei, M., Garza-Girón, R., Dominguez, L. A., et al. (2021). Short-term interaction between silent and devastating earthquakes in Mexico. *Nature Communications*, 12(1), 1–14. https://doi.org/10.1038/s41467-021-22326-6
- Dal Zilio, L., van Dinther, Y., Gerya, T., & Avouac, J. P. (2019). Bimodal seismicity in the Himalaya controlled by fault friction and geometry. Nature Communications, 10(1), 48. https://doi.org/10.1038/s41467-018-07874-8
- DeDontney, N., Rice, J. R., & Dmowska, R. (2012). Finite element modeling of branched ruptures including off-fault plasticity. Bulletin of the Seismological Society of America, 102(2), 541–562. https://doi.org/10.1785/0120110134
- Dieterich, J. H. (1979). Modeling of rock friction: 1. Experimental results and constitutive equations. *Journal of Geophysical Research*, 84(B5), 2161–2168. https://doi.org/10.1029/JB084iB05p02161
- Dieterich, J. H. (1981). Constitutive properties of faults with simulated Gouge. Mechanical Behavior of Crustal Rocks: The Handin Volume, 24, 103–120. https://doi.org/10.1029/gm024p0103
- England, P. C., & May, D. A. (2021). The global range of temperatures on convergent plate interfaces. *Geochemistry, Geophysics, Geosystems*, 22(8), 1–19. https://doi.org/10.1029/2021GC009849
- Erickson, B. A., Jiang, J., Barall, M., Lapusta, N., Dunham, E. M., Harris, R., et al. (2020). The community code verification exercise for simulating sequences of earthquakes and aseismic slip (SEAS). Seismological Research Letters, 91(2A), 874–890. https://doi.org/10.1785/0220190248
- Erickson, B. A., Jiang, J., Lambert, V., Barbot, S. D., Abdelmeguid, M., Almquist, M., et al. (2023). Incorporating full elastodynamic effects and dipping fault geometries in community code verification exercises for simulations of earthquake sequences and assismic slip (SEAS). *Bulletin of the Seismological Society of America*, 113(2), 499–523. https://doi.org/10.1785/0120220066

BIEMILLER ET AL. 22 of 24



Journal of Geophysical Research: Solid Earth

- 10.1029/2024JB029191
- Frank, W. B. (2016). Slow slip hidden in the noise: The intermittence of tectonic release. *Geophysical Research Letters*, 43(19), 10125–10133. https://doi.org/10.1002/2016GL069537
- Frank, W. B., Rousset, B., Lasserre, C., & Campillo, M. (2018). Revealing the cluster of slow transients behind a large slow slip event. *Science Advances*, 4(5), eaat0661. https://doi.org/10.1126/SCIADV.AAT0661
- Frank, W. B., Shapiro, N. M., Husker, A. L., Kostoglodov, V., Bhat, H. S., & Campillo, M. (2015). Along-fault pore-pressure evolution during a slow-slip event in Guerrero, Mexico. Earth and Planetary Science Letters, 413, 135–143. https://doi.org/10.1016/j.epsl.2014.12.051
- Frank, W. B., Shapiro, N. M., Husker, A. L., Kostoglodov, V., Romanenko, A., & Campillo, M. (2014). Using systematically characterized low-frequency earthquakes as a fault probe in Guerrero, Mexico. *Journal of Geophysical Research: Solid Earth*, 119(10), 7686–7700. https://doi.org/10.1002/2014JB011457
- Frank, W. B., Shapiro, N. M., Kostoglodov, V., Husker, A. L., Campillo, M., Payero, J. S., & Prieto, G. A. (2013). Low-frequency earthquakes in the Mexican sweet spot. *Geophysical Research Letters*, 40(11), 2661–2666. https://doi.org/10.1002/grl.50561
- Hardebeck, J. L. (2015). Stress orientations in subduction zones and the strength of subduction megathrust faults. Science, 349(6253), 1213–1216. https://doi.org/10.1126/SCIENCE.AAC5625
- Hardebeck, J. L., & Loveless, J. P. (2018). Creeping subduction zones are weaker than locked subduction zones. Nature Geoscience, 11(1), 60–64. https://doi.org/10.1038/s41561-017-0032-1
- Harris, R. A. (2004). Numerical simulations of large earthquakes: Dynamic rupture propagation on heterogeneous faults. Pure and Applied Geophysics, 161(11-12), 2171-2181. https://doi.org/10.1007/s00024-004-2556-8
- Hayes, G. P., Moore, G. L., Portner, D. E., Hearne, M., Flamme, H., Furtney, M., & Smoczyk, G. M. (2018). Slab2, a comprehensive subduction zone geometry model. *Science*. 362(6410), 58–61. https://doi.org/10.1126/science.aat4723
- Herrendörfer, R., Van Dinther, Y., Gerya, T., & Dalguer, L. A. (2015). Earthquake super cycle in subduction zones controlled by the width of the seismogenic zone. *Nature Geoscience*, 8(6), 471–474. https://doi.org/10.1038/NGEO2427
- Herrera, M. T., Crempien, J. G. F., Cembrano, J., & Moreno, M. (2024). Seismic cycle controlled by subduction geometry: Novel 3-D quasi-dynamic model of Central Chile megathrust. *Geophysical Journal International*, 237(2), 772–787. https://doi.org/10.1093/gji/ggae069
- Heuret, A., Lallemand, S., Funiciello, F., Piromallo, C., & Faccenna, C. (2011). Physical characteristics of subduction interface type seismogenic zones revisited. *Geochemistry, Geophysics, Geosystems*, 12(1), 1–26. https://doi.org/10.1029/2010GC003230
- Hubbard, J., Almeida, R., Foster, A., Sapkota, S. N., Bürgi, P., & Tapponnier, P. (2016). Structural segmentation controlled the 2015 MW 7.8
- Gorkha earthquake rupture in Nepal. *Geology*, 44(8), 639–642. https://doi.org/10.1130/G38077.1

 Husker, A. L., Kostoglodov, V., Cruz-Atienza, V. M., Legrand, D., Shapiro, N. M., Payero, J. S., et al. (2012). Temporal variations of non-valencia tempor (NVT) legations in the Maximum subdustion range. Finding the NVT event great. *Geographysics Geographysics Computation*
- volcanic tremor (NVT) locations in the Mexican subduction zone: Finding the NVT sweet spot. *Geochemistry, Geophysics, Geosystems,* 13(3). https://doi.org/10.1029/2011GC003916
- Jiang, J., Erickson, B. A., Lambert, V. R., Ampuero, J. P., Ando, R., Barbot, S. D., et al. (2022). Community-driven code comparisons for three-dimensional dynamic modeling of sequences of earthquakes and aseismic slip. *Journal of Geophysical Research: Solid Earth*, 127(3), e2021JB023519. https://doi.org/10.1029/2021JB023519
- Kostoglodov, V., Singh, S. K., Santiago, J. A., Franco, S. I., Larson, K. M., Lowry, A. R., & Bilham, R. (2003). A large silent earthquake in the Guerrero seismic gap, Mexico. Geophysical Research Letters, 30(15). https://doi.org/10.1029/2003GL017219
- Lavier, L. L., Tong, X., & Biemiller, J. (2021). The mechanics of creep, slow slip events and earthquakes in mixed brittle-ductile fault zones. Journal of Geophysical Research: Solid Earth, 126(2), e2020JB020325. https://doi.org/10.1029/2020JB020325
- Li, D., & Gabriel, A.-A. (2024). Linking 3D long-term slow-slip cycle models with rupture dynamics: The nucleation of the 2014 Mw 7.3 Guerrero, Mexico earthquake. AGU Advances, 5(2), e2023AV000979. https://doi.org/10.1029/2023AV000979
- Li, D., & Liu, Y. (2016). Spatiotemporal evolution of slow slip events in a nonplanar fault model for northern Cascadia subduction zone. *Journal of Geophysical Research: Solid Earth*, 121(9), 6828–6845. https://doi.org/10.1002/2016JB012857
- Li, D., & Liu, Y. (2017). Modeling slow-slip segmentation in Cascadia subduction zone constrained by tremor locations and gravity anomalies. Journal of Geophysical Research: Solid Earth, 122(4), 3138–3157. https://doi.org/10.1002/2016JB013778
- Li, D., & Liu, Y. (2021). Cascadia megathrust earthquake rupture model constrained by geodetic fault locking. *Philosophical Transactions of the Royal Society A*, 379(2196), 20200135. https://doi.org/10.1098/RSTA.2020.0135
- Liu, Y., & Rice, J. R. (2005). Assismic slip transients emerge spontaneously in three-dimensional rate and state modeling of subduction earthquake sequences. *Journal of Geophysical Research*, 110(8), 1–14. https://doi.org/10.1029/2004JB003424
- Liu, Y., & Rice, J. R. (2007). Spontaneous and triggered aseismic deformation transients in a subduction fault model. *Journal of Geophysical Research*, 112(9). https://doi.org/10.1029/2007JB004930
- Liu, Y., & Rice, J. R. (2009). Slow slip predictions based on granite and gabbro friction data compared to GPS measurements in northern Cascadia. Journal of Geophysical Research, 114(B9), B09407. https://doi.org/10.1029/2008JB006142
- Ma, S., & Hirakawa, E. T. (2013). Dynamic wedge failure reveals anomalous energy radiation of shallow subduction earthquakes. Earth and Planetary Science Letters, 375, 113–122. https://doi.org/10.1016/j.epsl.2013.05.016
- Ma, S., & Nie, S. (2019). Dynamic wedge failure and along-arc variations of Tsunamigenesis in the Japan trench margin. Geophysical Research Letters, 46(15), 8782–8790. https://doi.org/10.1029/2019GL083148
- Mark, H. F., Behn, M. D., Olive, J. A., & Liu, Y. (2018). Controls on mid-ocean ridge normal fault seismicity across spreading rates from rate-and-state friction models. *Journal of Geophysical Research: Solid Earth*, 123(8), 6719–6733. https://doi.org/10.1029/2018JB015545
- Melnick, D., Moreno, M., Motagh, M., Cisternas, M., & Wesson, R. L. (2012). Splay fault slip during the Mw 8.8 2010 Maule Chile earthquake. Geology, 40(3), 251–254. https://doi.org/10.1130/G32712.1
- Mitsui, N., & Hirahara, K. (2006). Slow slip events controlled by the slab dip and its lateral change along a trench. Earth and Planetary Science Letters, 245(1–2), 344–358. https://doi.org/10.1016/j.epsl.2006.03.001
- Muldashev, I. A., & Sobolev, S. V. (2020). What controls maximum magnitudes of giant subduction earthquakes? Geochemistry, Geophysics, Geosystems, 21(9), https://doi.org/10.1029/2020GC009145
- Oeser, J., Bunge, H. P., & Mohr, M. (2006). Cluster design in the Earth Sciences Tethys. In *Lecture Notes in Computer Science (Including Subseries Lecture Notes in Artificial Intelligence and Lecture Notes in Bioinformatics)*, 4208 LNCS (pp. 31–40). Berlin, Heidelberg: Springer Berlin Heidelberg. https://doi.org/10.1007/11847366_4
- Ong, S. Q. M., Barbot, S., & Hubbard, J. (2019). Physics-based scenario of earthquake cycles on the Ventura thrust system, California: The effect of variable friction and fault geometry. Pure and Applied Geophysics, 176(9), 3993–4007. https://doi.org/10.1007/s00024-019-02111-9
- Perez-Silva, A., Kaneko, Y., Savage, M., Wallace, L., Li, D., & Williams, C. (2022). Segmentation of shallow slow slip events at the Hikurangi subduction zone explained by along-strike changes in fault geometry and plate convergence rates. *Journal of Geophysical Research: Solid Earth*, 127(1), e2021JB022913. https://doi.org/10.1029/2021JB022913

BIEMILLER ET AL. 23 of 24



Journal of Geophysical Research: Solid Earth

- 10.1029/2024JB029191
- Perez-Silva, A., Li, D., Gabriel, A. A., & Kaneko, Y. (2021). 3D modeling of long-term slow slip events along the flat-slab segment in the Guerrero seismic gap, Mexico. *Geophysical Research Letters*, 48(13), 1–27. https://doi.org/10.1029/2021GL092968
- Philibosian, B., & Meltzner, A. J. (2020). Segmentation and supercycles: A catalog of earthquake rupture patterns from the Sumatran Sunda megathrust and other well-studied faults worldwide. *Quaternary Science Reviews*, 241, 106390. https://doi.org/10.1016/j.quascirev.2020. 106390
- Plescia, S. M., & Hayes, G. P. (2020). Geometric controls on megathrust earthquakes. *Geophysical Journal International*, 222(2), 1270–1282. https://doi.org/10.1093/GJI/GGAA254
- Qiu, Q., Hill, E. M., Barbot, S., Hubbard, J., Feng, W., Lindsey, E. O., et al. (2016). The mechanism of partial rupture of a locked megathrust: The role of fault morphology. *Geology*, 44(10), 875–878. https://doi.org/10.1130/G38178.1
- Ramos, M. D., Thakur, P., Huang, Y., Harris, R. A., & Ryan, K. J. (2022). Working with dynamic earthquake rupture models: A practical guide. Seismological Research Letters, 93(4), 2096–2110. https://doi.org/10.1785/0220220022
- Rice, J. R. (1993). Spatio-temporal complexity of slip on a fault. *Journal of Geophysical Research*, 98(B6), 9885–9907. https://doi.org/10.1029/93JB00191
- Rogers, G., & Dragert, H. (2003). Episodic tremor and slip on the Cascadia subduction zone: The chatter of silent slip. Science, 300(5627), 1942–1943. https://doi.org/10.1126/science.1084783
- Romanet, P., Bhat, H. S., Jolivet, R., & Madariaga, R. (2018). Fast and slow slip events emerge due to fault geometrical complexity. *Geophysical*
- Research Letters, 45(10), 4809–4819. https://doi.org/10.1029/2018GL077579

 Romanet, P., Sato, D. S. K., & Ando, R. (2020). Curvature, a mechanical link between the geometrical complexities of a fault: Application to bends, kinks and rough faults. Geophysical Journal International, 223(1), 211–232. https://doi.org/10.1093/gji/ggaa308
- Rubin, A. M. (2008). Episodic slow slip events and rate-and-state friction. *Journal of Geophysical Research*, 113(11). https://doi.org/10.1029/
- Rubin, A. M., & Ampuero, J. P. (2005). Earthquake nucleation on (aging) rate and state faults. *Journal of Geophysical Research*, 110(11), 1–24.
- https://doi.org/10.1029/2005JB003686

 Ruina, A. (1983). Slip instability and state variable friction laws. *Journal of Geophysical Research*, 88(B12), 10359–10370, https://doi.org/10.
- 1029/JB088iB12p10359
 Sathiakumar, S., & Barbot, S. (2021). The stop-start control of seismicity by fault bends along the Main Himalayan Thrust. *Communications Earth*
- Sathiakumar, S., & Barbot, S. (2021). The stop-start control of seismicity by fault bends along the Main Himalayan Thrust. Communications Earth and Environment, 2(1), 87. https://doi.org/10.1038/s43247-021-00153-3
- Sathiakumar, S., Barbot, S., & Hubbard, J. (2020). Earthquake cycles in fault-bend folds. *Journal of Geophysical Research: Solid Earth*, 125(8), e2019JB018557. https://doi.org/10.1029/2019JB018557
- Schellart, W. P., & Rawlinson, N. (2013). Global correlations between maximum magnitudes of subduction zone interface thrust earthquakes and physical parameters of subduction zones. *Physics of the Earth and Planetary Interiors*, 225, 41–67. https://doi.org/10.1016/J.PEPI.2013.10.001
- Shibazaki, B., Matsuzawa, T., Tsutsumi, A., Ujiie, K., Hasegawa, A., & Ito, Y. (2011). 3D modeling of the cycle of a great Tohoku-oki earth-quake, considering frictional behavior at low to high slip velocities. *Geophysical Research Letters*, 38(21). https://doi.org/10.1029/
- Skarbek, R. M., Rempel, A. W., & Schmidt, D. A. (2012). Geologic heterogeneity can produce assismic slip transients. Geophysical Research Letters, 39(21). https://doi.org/10.1029/2012GL053762
- Tal, Y., & Hager, B. H. (2018). Dynamic mortar finite element method for modeling of shear rupture on frictional rough surfaces. Computational Mechanics, 61(6), 699–716. https://doi.org/10.1007/s00466-017-1475-3
- Tal, Y., Hager, B. H., & Ampuero, J. P. (2018). The effects of fault roughness on the earthquake nucleation process. *Journal of Geophysical Research: Solid Earth*, 123(1), 437–456. https://doi.org/10.1002/2017JB014746
- Ulrich, T., Gabriel, A.-A., & Madden, E. H. (2022). Stress, rigidity and sediment strength control megathrust earthquake and tsunami dynamics. Nature Geoscience, 15(1), 67–73. https://doi.org/10.1038/s41561-021-00863-5
- Uphoff, C., May, D., Gabriel, A.-A., & Biemiller, J. (2024). Tandem: A scalable discontinuous Galerkin code on unstructured curvilinear grids for linear elasticity problems and sequences of earthquakes and aseismic slip. dmay/seas-checkpoint-greenfunc. September 2, 2021 Release (Version 1.0) [Software]. Zenodo. https://doi.org/10.5281/zenodo.12588421
- Uphoff, C., May, D. A., & Gabriel, A.-A. (2023). A discontinuous Galerkin method for sequences of earthquakes and aseismic slip on multiple faults using unstructured curvilinear grids. Geophysical Journal International, 233(1), 586–626. https://doi.org/10.1093/gji/ggac467
- van Zelst, I., Rannabauer, L., Gabriel, A. A., & van Dinther, Y. (2022). Earthquake rupture on multiple splay faults and its effect on tsunamis. Journal of Geophysical Research: Solid Earth, 127(8), e2022JB024300. https://doi.org/10.1029/2022JB024300
- Wallace, L. M. (2020). Slow slip events in New Zealand. Annual Review of Earth and Planetary Sciences, 48(1), 175–203. https://doi.org/10.1146/annurey-earth-071719-055104
- Walton, M. A. L., Staisch, L. M., Dura, T., Pearl, J. K., Sherrod, B., Gomberg, J., et al. (2021). Toward an integrative geological and geophysical view of Cascadia subduction zone earthquakes. Annual Review of Earth and Planetary Sciences, 49(1), 367–398. https://doi.org/10.1146/annurev-earth-071620-065605
- Wang, K., & Bilek, S. L. (2011). Do subducting seamounts generate or stop large earthquakes? Geology, 39(9), 819–822. https://doi.org/10.1130/G31856.1
- Wirth, E. A., Sahakian, V. J., Wallace, L. M., & Melnick, D. (2022). The occurrence and hazards of great subduction zone earthquakes. *Nature Reviews Earth & Environment*, 3(2), 125–140. https://doi.org/10.1038/s43017-021-00245-w
- Yu, H., Liu, Y., Yang, H., & Ning, J. (2018). Modeling earthquake sequences along the Manila subduction zone: Effects of three-dimensional fault geometry. *Tectonophysics*, 733(August 2017), 73–84. https://doi.org/10.1016/j.tecto.2018.01.025

BIEMILLER ET AL. 24 of 24